

LEBANESE AMERICAN UNIVERSITY

Numerical Simulation of Two-Phase Boiling
Flows in Macro and Micro-scale Channels

By

Michael Maalouly

A Thesis

Submitted in partial fulfilment of requirements for
the degree of Master of Science in Engineering

School of Engineering

December 2020

© 2020

Michael Maalouly

All Rights Reserved

THESIS APPROVAL FORM

Student Name: Michael Maalouly I.D. #: 201401629

Thesis Title : Numerical Simulation of Two-Phase Boiling Flows in Macro and Micro-scale Channels

Program: Master of Science in Mechanical Engineering

Department: Industrial and Mechanical Engineering

School: Engineering

The undersigned certify that they have examined the final electronic copy of this thesis and approved it in Partial Fulfillment of the requirements for the degree of:

Master of Science in the major of Mechanical Engineering

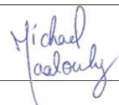
Thesis Advisor's Name	Amne El Cheikh	Signature	 <small>Digitally signed by Amne El Cheikh Date: 2020.12.01 16:20:35 +02'00'</small>	DATE: 01 / 12 / 2020
				Day Month Year
Committee Member's Name	Barbar Akle	Signature	 <small>Digitally signed by Barbar Akle DN: cn=Barbar Akle, o=Lebanese American University, ou=Assistant Provost, email=barbar.akle@lau.edu.lb, c=LB Date: 2020.12.02 17:29:28 +02'00'</small>	DATE: 02 / 12 / 2020
				Day Month Year
Committee Member's Name	Michel Khoury	Signature	 <small>Digitally signed by Michel Elkhoury DN: cn=Michel Elkhoury, o=LAU, ou, email=mkhoury@lau.edu.lb, c=LB Date: 2020.12.02 12:14:49 +02'00'</small>	DATE: 02 / 12 / 2020
				Day Month Year

THESIS COPYRIGHT RELEASE FORM

LEBANESE AMERICAN UNIVERSITY NON-EXCLUSIVE DISTRIBUTION LICENSE

By signing and submitting this license, you (the author(s) or copyright owner) grants the Lebanese American University (LAU) the non-exclusive right to reproduce, translate (as defined below), and/or distribute your submission (including the abstract) worldwide in print and electronic formats and in any medium, including but not limited to audio or video. You agree that LAU may, without changing the content, translate the submission to any medium or format for the purpose of preservation. You also agree that LAU may keep more than one copy of this submission for purposes of security, backup and preservation. You represent that the submission is your original work, and that you have the right to grant the rights contained in this license. You also represent that your submission does not, to the best of your knowledge, infringe upon anyone's copyright. If the submission contains material for which you do not hold copyright, you represent that you have obtained the unrestricted permission of the copyright owner to grant LAU the rights required by this license, and that such third-party owned material is clearly identified and acknowledged within the text or content of the submission. IF THE SUBMISSION IS BASED UPON WORK THAT HAS BEEN SPONSORED OR SUPPORTED BY AN AGENCY OR ORGANIZATION OTHER THAN LAU, YOU REPRESENT THAT YOU HAVE FULFILLED ANY RIGHT OF REVIEW OR OTHER OBLIGATIONS REQUIRED BY SUCH CONTRACT OR AGREEMENT. LAU will clearly identify your name(s) as the author(s) or owner(s) of the submission, and will not make any alteration, other than as allowed by this license, to your submission.

Name: Michael Maalouly

Signature: 

Date: 11/30/2020

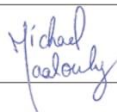
PLAGIARISM POLICY COMPLIANCE STATEMENT

I certify that:

1. I have read and understood LAU's Plagiarism Policy.
2. I understand that failure to comply with this Policy can lead to academic and disciplinary actions against me.
3. This work is substantially my own, and to the extent that any part of this work is not my own I have indicated that by acknowledging its sources.

Name: Michael Maalouly

Signature:



Date: 11/30/2020

The work that I have done is dedicated to my loving parents and siblings who have
always supported me.

It is specially dedicated to my father who was my role model and inspiration to
become a mechanical engineer.

Acknowledgement

This project would not have been possible without the support of many people. Firstly, I would like to thank Dr. Barbar Akle and Martin Gastal for making this project possible as it is a Lebanese American University – CERN/CMS collaboration. Secondly, a big part of this project would not have been achievable without the help and guidance of Dr. Mauro Carnevale. He is the main reason why this project was able to prosper, he has endured my nonstop questions and answered each one with patience. I started this project not knowing how to operate OpenFOAM, but with the help of Dr. Carnevale and Dr. Nicola Casari, I was able to become a proficient user of OpenFOAM to say the least. Last but not least, many thanks to my advisor, Dr. Amne El Cheikh, who offered me guidance and support throughout this process.

Numerical Simulation of Two-Phase Boiling Flows in Macro and Micro-scale Channels

Michael Maalouly

Abstract

Two-phase boiling flows are used in a wide range of engineering applications. One of the most common applications is cooling systems. A refrigerant is injected into a closed-loop under saturation conditions extracting the unwanted heat from the corresponding system and boiling as a consequence. However, flow boiling is a complex process governed by several flow characteristics making it challenging to predict. It is strongly related to the turbulence and shear stress occurring between the two phases. Correlations are usually used to model this process. These correlations are based on global averaged parameters in a certain range of operating conditions, while boiling is also dependent on local effects. Thus, the implementation of a more sophisticated numerical approach is mandatory. Computational Fluid Dynamics (CFD) can provide the needed local flow characteristics to predict all aspects of boiling. In this study, a two-phase model implemented in an open-source CFD solver has been tested on two different fluids: Freon R12 and Carbon Dioxide CO₂. R12 was chosen since it is one of the most common fluids employed in cooling technologies and its behaviour has been widely assessed experimentally. In addition, CO₂ fluid has been selected as it is the new refrigerant with promising characteristics to replace CFCs such as R12. In particular, CERN/CMS is heading in that direction as they are updating their detector cooling system to CO₂ evaporative cooling. The CFD model has been tested for the two fluids in different configurations and under various levels of simplification of the model. This work provides a detailed analysis of the key physical aspects dominating the boiling process such as turbulence and buoyancy effects. Finally, some recommendations on best practices in modelling boiling flows are provided.

Keywords: CFD, boiling flows, macro-channel, micro-channel, two-phase flows, OpenFOAM, CO₂, R12, CERN, CMS, void fraction, turbulence

Table of Contents

Chapter	Page
I-Introduction	1
II-Literature Review	5
2.1 R12 Flow Boiling	5
2.2 Flow Patterns.....	6
2.3 CO ₂ Flow Boiling.....	8
III-Mathematical Modelling.....	12
3.1 Flow Governing Equations	14
3.2 Interfacial Forces.....	16
3.2.1 Drag Force.....	16
3.2.2 Lift Force.....	16
3.2.3 Wall Lubrication	17
3.2.4 Turbulent Dispersion Force	17
3.2.5 Virtual Mass Force.....	18
3.3 Phase Change Model.....	18
3.3.1 Boiling Model	18
3.3.2 Phase Change Model A.....	18
3.3.3 Phase Change Model B	19
3.3.4 Bubble Diameter	19
3.4 Turbulence Model	19
3.4.1 Turbulence Equations for the Liquid Phase	19
3.4.2 Turbulence Equations for the Gaseous Phase	20
IV-Methodology	21
4.1 OpenFOAM	21
4.1.1 OpenFOAM Brief	21
4.1.2 Two-Phase Solver	22
4.2 Test Cases	23
4.2.1 DEBORA 6 Experiment.....	23
4.2.2 CO ₂ CERN Experiment	25
4.3 Numerical Approach	27
4.3.1 R12 Simulations	27
4.3.2 CO ₂ Simulations.....	30
V-Results and Discussion.....	35
5.1 R12 Results	35

5.1.1 Time and Mesh Sensitivity Analysis	35
5.1.2 $C_{\epsilon 3}$ Sensitivity Analysis	37
5.1.3 Turbulence Quantities Assessment	39
5.2 CO ₂ Results	43
5.2.1 Time and Mesh Sensitivity Analysis	44
5.2.2 Pressure drop Results	45
5.2.3 Evaluation of the CO ₂ Flow at Different Sections	48
VI-Conclusion	51
References	52
Appendix A	54
Appendix B	55
Appendix C	56

Table of Figures

Figure 1 Simplified schematic of the 2PACL system.....	3
Figure 2 Horizontal two-phase flow patterns.....	7
Figure 3 Vertical two-phase flow patterns.....	7
Figure 4 Pressure-Temperature curve.....	12
Figure 5 Pure substance P-v diagram.....	13
Figure 6 OpenFOAM structural overview.....	21
Figure 7 Outline of a basic OpenFOAM directory.....	22
Figure 8 DEBORA 6 pipe configuration.....	24
Figure 9 Data extraction layout.....	25
Figure 10 Schematic of CERN/CMS detector cooling system.....	26
Figure 11 CERN experimental setup.....	27
Figure 12 Pressure drop section schematic.....	27
Figure 13 2D-axisymmetric wedge.....	28
Figure 14 Direction of mesh vectors for the R12 wedge geometry.....	28
Figure 15 Mesh cross section for the R12 medium mesh.....	29
Figure 16 Axial view of the medium mesh.....	29
Figure 17 Initial geometry for the CO ₂ simulations.....	31
Figure 18 Section for CO ₂ data extraction (initial geometry).....	31
Figure 19 2D vs 3D for CO ₂ simulations.....	32
Figure 20 CO ₂ simulations modified geometry.....	32
Figure 21 Data extraction sections from the CO ₂ simulations.....	33
Figure 22 CO ₂ O-type mesh structure.....	33
Figure 23 Direction of mesh vectors for the CO ₂ cylindrical geometry.....	34
Figure 24 Void Fraction mesh sensitivity analysis for the R12 simulations.....	36
Figure 25 Temperature mesh sensitivity analysis for the R12 simulations.....	36
Figure 26 Effect of $C\epsilon_3$ on the void fraction distribution in the R12 simulations.....	38
Figure 27 Comparison of numerical void fraction results and experimental data.....	38
Figure 28 Liquid and gas turbulence comparison in R12 simulations.....	40
Figure 29 Comparison of reactingTwoPhaseEulerFoam phase change models.....	41
Figure 30 liquid turbulence results for the liquid phase change model B.....	41
Figure 31 R12 temperature distribution for the different phase change models.....	42
Figure 32 Comparison of numerical temperature results and experimental data.....	43
Figure 33 Pressure drop mesh sensitivity analysis for the CO ₂ simulations.....	44
Figure 34 $C\epsilon_3$ sensitivity analysis for the CO ₂ microchannel simulations.....	45
Figure 35 CO ₂ pressure drop results for the 240 mm channel.....	46
Figure 36 Visualization of Leidenfrost effect.....	47
Figure 37 CO ₂ pressure drop results for the 500 mm channel.....	47
Figure 38 CO ₂ void fraction and turbulent energy at different sections of the pipe..	48
Figure 39 CO ₂ void fraction visualization at different pipe sections.....	49
Figure 40 DEBORA 6 radial temperature distribution.....	54
Figure 41 DEBORA 6 radial gas void fraction distribution.....	54
Figure 42 CO ₂ pressure drop experimental data.....	55

List of Tables

Table 1 GWP and ODP of common refrigerants	2
Table 2 Literature Review Summary	10
Table 3 DEBORA 6 experimental conditions.....	23
Table 4 CO ₂ experimental conditions for chosen test cases	26
Table 5 Mesh element configurations for the R12 simulations	29
Table 6 Thermophysical properties for the R12 simulations	30
Table 7 Mesh element configurations for the CO ₂ simulations	34
Table 8 Thermophysical properties for the CO ₂ simulations.....	34

Chapter 1

Introduction

All systems be they chemical, electrical and/or mechanical dissipate heat. This heat, if not extracted properly, can damage the device's components. For example, the heat dissipated by a car engine is so large that it can cause the piston to get welded to the cylinder, demonstrating that the surface temperature of the piston reached 204°C or more. Additionally, a common cause of failure for electrical components is overheating: leaving a mobile phone out in the midday sun for hours will impose strain on its battery. Thus, the need for efficient heat exchangers and cooling systems. Heat exchangers, as their name suggests, are systems used to transfer heat from one fluid to another. These two fluids are usually separated by a solid wall through which the transfer occurs. Heat exchangers are used in refrigeration cycles to move unwanted heat from one area to another one where it can be disposed of or reused. Refrigeration cycles are fundamentally mechanical systems that transfer heat from a high temperature place to another lower temperature one by means of a working fluid, called refrigerant.

Heat exchangers and refrigeration cycles have greatly evolved throughout the years. The coefficient of performance (COP) of refrigeration systems has been enhanced by boosting component efficiencies and employing the most appropriate working fluid. The performance of the entire refrigeration system depends mainly on the behaviour of the working fluid. One important phenomenon is experienced by the working fluid as it passes in the evaporator, extracts heat and boils. Being able to predict flow properties during the boiling process will aid in the optimization of the system. Numerical simulations, empirical methods and predictive methods are utilized to study the boiling phenomena. These approaches are validated for the most commonly used refrigerant groups such as Chlorofluorocarbons (CFCs), Hydrochlorofluorocarbons (HCFCs), Hydrofluorocarbons (HFCs). However, nowadays, most CFCs, HCFCs and HFCs are banned because of their high Ozone Depleting Potential (ODP) and Global Warming Potential (GWP). Table 1 shows examples of popular refrigerants and their GWPs and ODPs (Kadhum, 2016). The two most eco-friendly refrigerants are Carbon Dioxide - R744 (CO_2) and Ammonia, but the latter is toxic in the case of chemical

leak. That is why current refrigeration systems are shifting towards the use of natural refrigerants. CO₂ being non-flammable, non-toxic with a zero ODP and a GWP of one, is considered an adequate refrigerant to use in modern refrigeration systems.

Table 1 GWP and ODP of common refrigerants

Working Fluid	GWP	ODP
R11	4750	1
R134a	1300	0
R245fa	950	0
R1234ze	6	0
R123	77	0.02
R1234yf	4.4	0
R245ca	726	0
R600 Butane	20	0
R21	151	0.04
R22	1790	0.055
R142b	2220	0.06
R114	9180	0.58
R113	4800	0.8
R12	10900	0.82
CO₂ (R744)	1	0
Ammonia	1	0

Moreover, the new generation of refrigeration systems are more compact making the use of macro-scale channels to circulate the refrigerant no longer feasible. State-of-the-art systems are based on micro-scale channels in which the flow is not always very well-understood due to the effect of confinement which is neglected in most predictive methods. A great example of a novel cooling system is the two-phase accumulator-controlled loop (2PACL) system in Figure 1 which is implemented at CERN to extract heat from the Compact Muon Solenoid (CMS) detector (Bhanot et al., 2020). This system is inspired by the system used in the International Space Station to cool the Alpha Magnetic Spectrometer. The state of the fluid is dictated by an accumulator which controls the system pressure, and consequently the temperature. Liquid CO₂ is

transported in a sensitive region near its boiling point at a saturation temperature of -40°C . Uncertainties in the flow behaviour can disrupt the system operation.

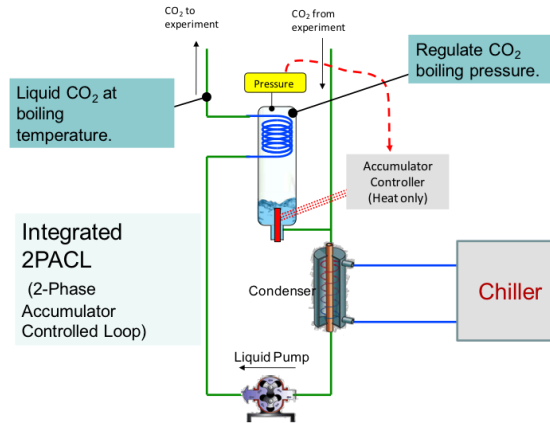


Figure 1 Simplified schematic of the 2PACL system

Producing reliable and sustainable correlations to predict flow properties requires the availability of a large amount of experimental data. The experimental setup which can generate this data set is expensive both financially and logistically. Additionally, it is very time consuming to conduct the necessary experiments.

One of the main advantages of numerical simulations is the significant reduction in the time and cost required to produce results. With the recent advances in computing power, researchers are able to simulate most unorthodox conditions with a minimal cost. For fluid dynamics, the Finite Volume Method carries the legacy of solving the Navier-Stokes equations. CFD is the branch of computational physics that utilizes the aforementioned numerical method to solve fluid dynamics problems. The solution technique consists of dissecting the domain and applying the governing equations on each small element. Nevertheless, boiling flows are still considered very complex systems to solve with conventional CFD packages. The underlying cause of this complexity is the necessity of employing liquid-gas interfacial equations in addition to solving transport equations and energy equations for each phase. Hence, a boiling flow specific Computational Fluid Dynamics (CFD) model is required. In this work, an open source CFD software called OpenFOAM is used since it is customizable and allows the user to dictate all aspects of the problem.

Based on the above, this study aims to simulate two-phase boiling flows in macro and micro-scale channels using OpenFOAM. A best practice for boiling simulations will be compiled based on a series of sensitivity analyses. Having a reliable CFD model that can predict the flow characteristics accurately will help improve the available correlations used to design cooling systems.

To be able to achieve the above-mentioned goal, the following objectives need to be met. Each objective corresponds to a chapter in this manuscript, starting from Chapter 2 to Chapter 6.

1. Performing a detailed literature review to showcase what has been done in terms of correlations and CFD simulations to model boiling flows.
2. Elaborating on the mathematical modelling needed to understand the physics of the flow.
3. Numerically recreating the boiling flow in the most adequate manner and simplifying the problem so that it can be approached using CFD.
4. Understanding and analyzing the flow characteristics by looking at the flow fields such as velocity, pressure, temperature, turbulence and void fraction.
5. Concluding with the lessons learned from the evaluation of the flow parameters and complying a set of recommendations for best practices when modelling boiling flows.

Chapter 2

Literature Review

Understanding the behaviour of two-phase boiling flows is essential to the optimization of evaporation-based cooling systems. Therefore, several experiments have been conducted to better understand the mechanics of the boiling process. In this chapter, few experimental studies that are relevant to this thesis will be summarized.

2.1 R12 Flow Boiling

A research group at the Commission for Atomic Energy and Alternative Energies (CEA) in Grenoble conducted tests on Freon R12 boiling flows in a vertical tube. The facility that is used to conduct these experiments is known as the DEBORA facility, hence the tests are now known as the DEBORA tests. As a result, a large data bank of local temperature, void fraction and bubble diameter measurements was collected. The test section is a 5-meter-long tube with a diameter of 19.2 mm, this tube is classified under the macro-scale category. Data have been extracted via an optical probe positioned at 4.485 meters from the section inlet. The authors guaranteed the consistency of the data by doing an internal check, which consisted of cross examining the liquid temperature profiles with the mixture quality. Then, the same temperature profiles were proven to be consistent with the system's energy balance. The DEBORA 6 temperature and void fraction data will be essential to the validation of the OpenFOAM solver used in this study. This data has been utilized to benchmark a number of numerical methods aimed to predict boiling flows. (Garnier et al., 2001)

Another study conducted at CEA Grenoble, explored the use of the CATHARE code, a thermohydraulic CFD tool created under a joint project between CEA, Electricity of France (EDF), Areva and the Institute for Radiological Protection and Nuclear Safety (IRSN), to simulate the multiphase boiling flow DEBORA cases. In this paper, the test cases of DEBORA 5, 6, 7 and 8 were selected. All 4 cases were first simulated using the default solver settings (Yao & Morel, 2002). The simulation results for the DEBORA 5 case exhibited the best agreement with the experimental data. Hence, this case was selected for a sensitivity study that aims to better understand and enhance the simulation results. The effect of two turbulence parameters was examined:

$C_{\varepsilon 3}$, a coefficient related to the dissipation of turbulence created by bubbles (Morel, 2015), and C_{DT} , a turbulent dispersion force coefficient. This article highlights the importance of turbulence in the development of two-phase flows. According to Yao and Morel (2002), $C_{\varepsilon 3}$ influences the liquid temperature profile, while C_{DT} affects the void fraction distribution. For $C_{\varepsilon 3} = 0.1$, the solver predicted the liquid temperature profile very well but was not able to predict the void fraction distribution. For $C_{DT} = 5$, CATHARE shows the least error when comparing the numerical void fraction distribution to the DEBORA 5 results; however, the temperature profile was poorly predicted. Only 2 values of $C_{\varepsilon 3}$ were evaluated so no clear trend can be identified. Three values of C_{DT} were assessed demonstrating that by increasing C_{DT} the liquid temperature increases in the tube center and stays unaffected near the wall. When looking at the void fraction distribution, it is clear that the turbulent dispersion force plays a significant role in determining the void fraction distribution.

ANSYS CFX-12's Euler/Euler modelling of R12 boiling flows has been evaluated by Krepper and Rzehak (2011). The results show a certain degree of agreement with the DEBORA experiments. The temperature is predicted accurately, but it is the simplest fluid property to predict, since the mixture and liquid temperatures are bound to hover around the saturation temperature due to the physics of the boiling flows. When looking at the void fraction profiles and the velocity profiles showcased, discrepancies start to show up, and the simulations become less reliable. One main issue is that the CFX-12 simulations underestimate the void fraction in the radial direction in most of the numerical data shown. In a two-phase boiling system, void fraction plays an important role. For example, in cooling systems, the efficiency of the evaporator is dictated by the quality of the mixture at its outlet.

2.2 Flow Patterns

Collier and Thome (1994) characterised the flow patterns when transition from single-phase liquid flows to single-phase vapour flows occurs in both vertical and horizontal tubes (Figure 2 and Figure 3). Each pattern has distinct features with different mixture properties, thus numerical simulations were conducted to better interpret the details of the flow.

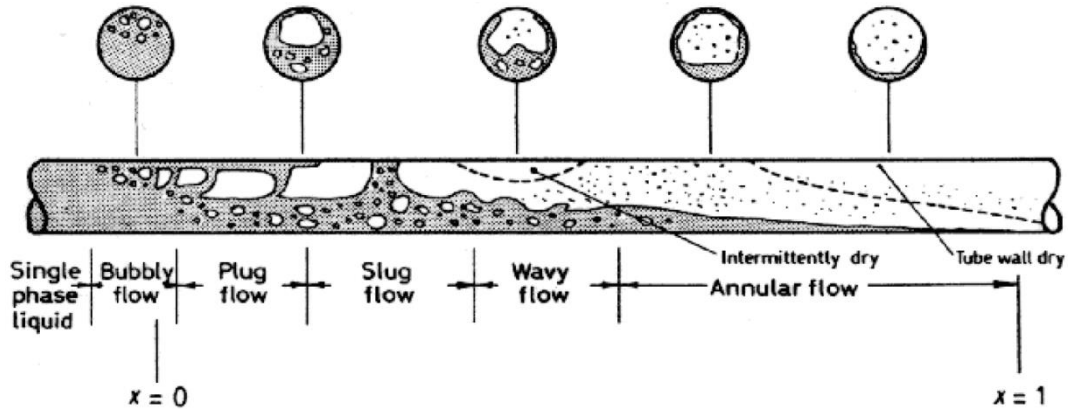


Figure 2 Horizontal two-phase flow patterns

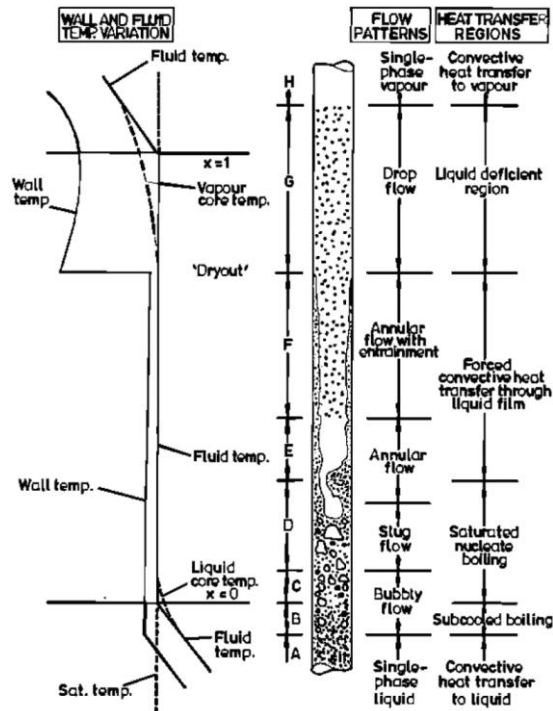


Figure 3 Vertical two-phase flow patterns

Zhuan and Wang (2012) simulated R134a and R22 flow boiling using Volume of Fluid (VOF) in a 0.5 mm horizontal microchannel at $T_{sat} = 30^{\circ}\text{C}$. The flow structure at different flow conditions was analyzed validating the observations illustrated in Figure 2 and Figure 3. The authors drew the following conclusions: increasing the heat and mass fluxes leads to early flow pattern transitions making it harder to capture the different flow properties; reducing the saturation temperatures makes flow pattern

transition occur at lower vapour qualities; bubble size and coalescence rate play an important role in the flow pattern transition. In Zhou et al (2013), COMSOL's VOF solver is also used to model water flow boiling in microchannels but the only deduced parameter is the wall temperature. A validation based on one parameter of the simulation does not give credibility to the competence of the solver. Likewise Ganaphathy et al (2013) modelled R134a two-phase flow with heat transfer using ANSYS Fluent 6.3.26's VOF solver and compared the results to those of empirical correlations. Therefore, the two-phase solver validation process is limited to the range of conditions over which the used correlations were developed.

Other studies were based on the introduction a specific flow pattern in the original flow field to better understand its effect on the flow characteristics. Magnini et al (2013) created a slug flow by inserting elongated vapour bubbles into a heated horizontal microchannel filled with liquid. This was done to capture the flow details around the bubble especially in the liquid film near the pipe wall. ANSYS Fluent 12's VOF was employed with some modifications. The bubble behaviour agreed with theoretical models enabling the authors to predict the local heat transfer accurately. As a follow up, the same research team ran an in depth numerical analysis on slug flow in microchannels using a newer version of the solver (ANSYS Fluent 14.5) with some inhouse enhancements (Magnini & Thome, 2016). This study lead to a set of non-dimensional groups related to bubble dynamics and heat transfer in slug flows.

Karayiannis and Mahmoud (2017) showed that the criteria for transition in both macro to micro scale tubes change based on the working fluid. In addition, the heat extraction capability of microchannel flow boiling was demonstrated by cooling an insulated gate bipolar transistor.

2.3 CO₂ Flow Boiling

The next generation of cooling systems seems to be heading towards CO₂ evaporative cooling, and CERN is pioneering research efforts to optimize these systems. Therefore, gaining insight on the behaviour of CO₂ under different conditions and geometries is crucial to improve the cooling process. Bhanot et al (2020) described the Two-Phase Accumulator-Controlled Loop (2PACL) cooling system used for Tracker cooling. Additionally, they developed and validated a one-dimensional

correlation-based simulation tool that helps with the system upgrades necessary to accommodate the detectors' increasing heat load.

However, as demonstrated in Mastrullo et al (2010) and Hellenschmidt and Petagna (2020), correlations cannot fully predict the behavior of CO₂, especially in microchannels. Mastrullo et al (2010) focused on the evaluation of heat transfer coefficient and pressure drop predictive methods for CO₂ boiling flows. The most renowned methods for predicting boiling flows were tested, and only one of them was able to estimate 70.4% of experimental data with an error lower than 30%.

Whereas Hellenschmidt and Petagna (2020) evaluated the pressure drop of low quality CO₂ boiling flows in three 200 mm long horizontal tubes with diameters of 2.15 mm, 1 mm and 0.5 mm. The tests carried out were at a wide range of saturation temperature, mass fluxes and heat fluxes. According to the experiments conducted, under the tested saturation temperature, the 2.15 mm channel falls under the macro-scale regime, the 0.5 mm falls under the micro-scale regime and the 1 mm exhibits transitional behaviour from macro to micro-scale flow. Moreover, this study shows that no correlation can fully predict the pressure drops of two-phase flows. The correlations are limited to the range of conditions under which they were assessed. Any model used to predict CO₂ boiling pressure drop in small channels needs to take into consideration the effect of saturation temperature and confinement. This article is particularly helpful as it provides the global pressure drop data used to benchmark the solver for CO₂ boiling flows in microchannels.

Table 2 presents a summary of relevant literature assessed above.

To sum things up, two-phase boiling flows are hard to predict using correlations especially for microchannels because some fundamental phenomena are not represented. Additionally, predictive methods work for a discrete range of conditions and for particular fluids. Furthermore, CFD numerical models tend to overestimate some properties and underestimate others. Therefore, the aim of this research is to provide guidelines for a comprehensive CFD solver able to predict the behaviour of two-phase boiling flows for different fluids under different conditions and geometries within a reasonable margin of error.

Table 2 Literature Review Summary

Title	Reference	Type	Fluid	Relevant Output
Local measurements on flow boiling of refrigerant 12 in a vertical tube	(Garnier et al., 2001)	Experimental	R12	Local temperature and void fraction data extracted at a radial profile. The data yielded by the DEBORA experiments is proven to be consistent and credible.
Flow boiling in microchannels: Fundamentals and applications	(Karayiannis & Mahmoud, 2017)	Experimental	R134a	Flow pattern transition criteria was identified for working fluids based on correlations.
Effects of saturation temperature on the boiling properties of carbon dioxide in small diameter pipes at low vapour quality: Pressure drop	(Hellenschmidt & Petagna, 2020)	Experimental	CO ₂	Experiments added relevant pressure drop data to the CO ₂ data bank and showed the effect of saturation temperature and confinement on CO ₂ flow boiling, especially in microchannels.
Convective Boiling and Condensation	(Collier & Thome, 1994)	Flow description	General	Full description of flow patterns for both vertical and horizontal boiling flows.
Mathematical Modeling of Disperse Two-Phase Flows	(Morel, 2015)	Mathematical modelling	General	Explanation of the modified k-e turbulence model relating $C_{\epsilon 3}$ to the dissipation of turbulence created by the wake of bubbles.
Carbon dioxide heat transfer coefficients and pressure drops during flow boiling: Assessment of predictive methods	(Mastrullo et al., 2010)	Correlations	CO ₂	Predictive methods are tested against experimental data to validate their use for CO ₂ boiling flows. Only one correlation yielded results with an adequate error margin.
Development and validation of a simulation tool for next generation detector cooling systems	(Bhanot et al., 2020)	Numerical modelling	CO ₂	Detailed description of the 2PACL cooling system used to extract heat from CERN Tracker.
Prediction of parameters distribution of upward boiling two-phase flow with two-fluid models	(Yao & Morel, 2002)	CFD modelling	R12	CATHARE is used to model R12 boiling flows. The simulations demonstrated the important role of turbulence in boiling flows, especially $C_{\epsilon 3}$ and C_{DT} .

CFD for subcooled flow boiling: Simulation of DEBORA experiments	(Krepper & Rzehak, 2011)	CFD modelling	R12	Validation of ANSYS CFX-12 for modelling R12 boiling flows. Void fraction profiles are underestimated.
Flow pattern of boiling in micro-channel by numerical simulation	(Zhuan & Wang, 2012)	CFD modelling	R134a & R22	VOF is used to model refrigerant flow boiling. The patterns match the described patterns in Collier and Thome (1994). Mass flux, heat flux and saturation temperature are exhibited to impact flow pattern transition.
Volume of fluid-based numerical modeling of condensation heat transfer and fluid flow characteristics in microchannels	(Ganapathy et al., 2013)	CFD modelling	R134a	ANSYS Fluent VOF two-phase flow modelling
Numerical investigation of hydrodynamics and heat transfer of elongated bubbles during flow boiling in a microchannel	(Magnini et al., 2013)	CFD modelling	R113, R134a & R245fa	In depth look at slug flow in microchannels using ANSYS Fluent VOF with an inhouse modification. Bubble behaviour agreed with theoretical calculations.
A CFD study of the parameters influencing heat transfer in microchannel slug flow boiling	(Magnini & Thome, 2016)	CFD modelling	R245fa	Advanced look into slug flow. A set of non-dimensional parameters related to the flow characteristics were identified.
Modeling of boiling flow in microchannels for nucleation characteristics and performance optimization	(Zhou et al., 2013)	CFD modelling	Water	COMSOL VOF is used to model boiling flow. The results showed a fair agreement with temperature experimental data but that is not enough to trust a solver.

Chapter 3

Mathematical Modelling

In this study, the flow enters the tube in a fully liquid state, then it reaches a heated area of the pipe providing enough energy to the flow until it boils. Once boiling begins, the flow becomes a mixture of two-phases: liquid and gas.

Boiling is the phenomena that occurs when a liquid reaches a temperature associated with a saturation pressure which is equal to the surrounding pressure. This temperature is the liquid's boiling point which is also known as the liquid saturation temperature. Each saturation temperature corresponds to a single saturation pressure as shown by the blue solid line in Figure 4. While on the blue line, vaporization is occurring and the two phases, liquid, and gas, coexist. A characteristic of boiling is that if the pressure of the system is maintained constant, the temperature also remains unchanged as shown by the dashed pink line noted as saturated liquid-vapour-region in Figure 5.

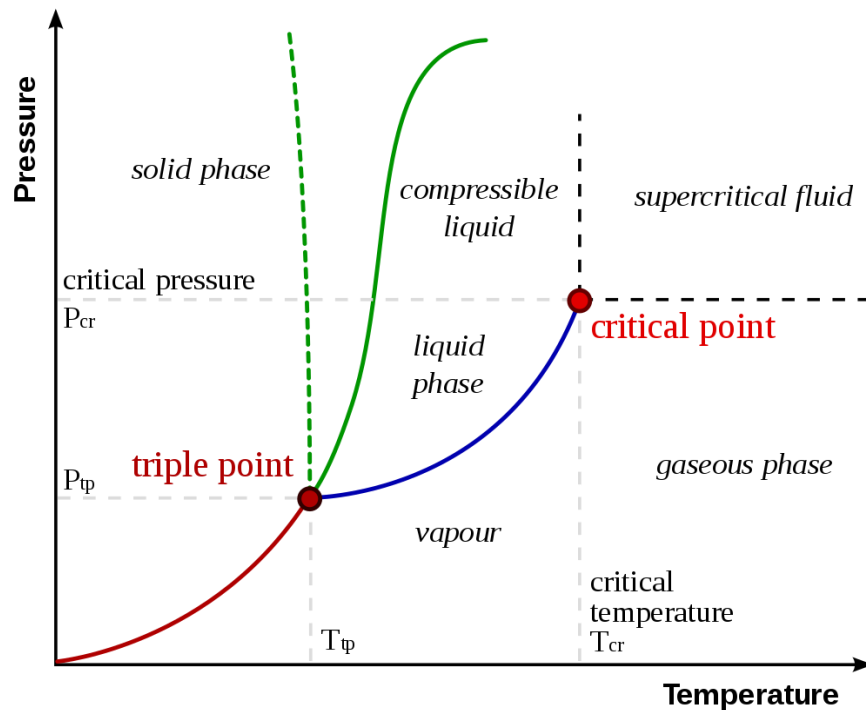


Figure 4 Pressure-Temperature curve

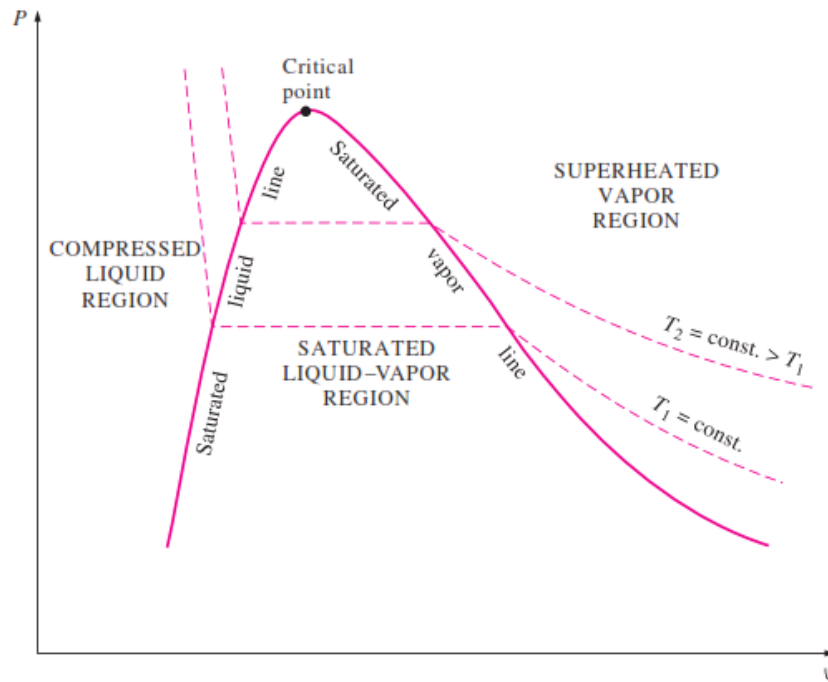


Figure 5 Pure substance P-v diagram

The two models for this kind of application are the Volume of Fluid (VOF) model and the Eulerian-Eulerian model. The VOF model shares the momentum equations between the two phases and is better for large interface mapping such as in stratified flows and predicting the motion of large bubbles in liquid. In the case under study in this thesis, flows are at low vapour qualities and each phase needs to have its dedicated momentum equations to better predict the flow characteristics. Therefore, the use of the Eulerian-Eulerian multiphase model is required to model the secondary dispersed phase in the continuous primary phase which are respectively, the gaseous phase and liquid phase. The importance of the Euler-Euler approach is its ability to solve the continuity, enthalpy, momentum and turbulence equations for each phase while tracking the volume fractions. More importantly, it takes into account the interfacial forces between phases allowing for better modelling of two-phase flows. Additionally, the model allows for mass and heat transfer between phases through boiling models. These aspects are what make the Eulerian-Eulerian Model the most adequate for this research project.

In this chapter, the flow governing equations, interfacial forces models, boiling model and turbulence model are going to be showcased and thoroughly described.

3.1 Flow Governing Equations

The governing equations for two-phase flows are similar to ones of single-phase flows with some modifications to include the phase volume fraction. The continuity equation can be expressed as:

$$\frac{\partial \alpha_k}{\partial t} + \nabla \cdot (\alpha_k \vec{U}_k) = \frac{\Gamma_{ki} - \Gamma_{ik}}{\rho_k} \quad (1)$$

Where k represents the main phase for which the equation is being solved, it can be either liquid (l) or gas (g), and i denotes the non- k phase. ρ , α , and U are the density, volume fraction and velocity respectively. Γ_{lg} is to the condensation rate per unit volume while Γ_{gl} is the evaporation rate per unit volume. Evaporation in the simulations is caused by the boiling process which starts from a nucleation site at the heated wall. Condensation is the only phase change possible at the interface between phases because the liquid is entering near saturation temperature and the transformed gas stays saturated. In real life boiling this might seem odd, since evaporation and condensation do not take place at the same point. However, numerically, there is a possibility of having a cell near the wall containing the two phases where condensation of the gas and evaporation of the liquid are concurring.

As we are only dealing with two phases of the same species, solving one continuity equation is sufficient. If the continuity equation is solved for the liquid phase and the liquid volume fraction is calculated, one can deduce the volume fraction of the gas from the following equation:

$$\alpha_i = 1 - \alpha_k \quad (2)$$

In the case mentioned above it becomes

$$\alpha_g = 1 - \alpha_l \quad (3)$$

The inverse can also be done, i.e. solving the continuity for the gaseous phase and then calculate the liquid volume fraction using equation (2).

Moving on to the momentum equation for a phase k :

$$\begin{aligned}
& \frac{\partial \alpha_k \vec{U}_k}{\partial t} + \nabla \cdot (\alpha_k \vec{U}_k \vec{U}_k) \\
& = -\nabla \cdot (\alpha_k (\bar{\bar{R}}_k + \bar{\bar{R}}_k^t)) - \frac{\alpha_k}{\rho_k} \vec{\nabla} p + \alpha_k \vec{g} + \frac{\vec{M}_k}{\rho_k} \\
& + \frac{\Gamma_{ki} \vec{U}_i - \Gamma_{ik} \vec{U}_k}{\rho_k}
\end{aligned} \tag{4}$$

Where the first term on the right hand side (RHS) corresponds to the combined viscous and turbulent stress. The second term represents the pressure drop across the modelled geometry. The third term accounts for gravity. The fourth term in the RHS is of particular importance because it represents the sum of the interfacial forces per unit volume which will be examined afterwards in section 3.2. Lastly, the fourth term corresponds to the change in momentum caused by phase change.

The stress term can be rewritten as a function of the fluid properties, turbulent kinetic energy and velocity (Boussinesq, 1897).

$$\bar{\bar{R}}_k^{eff} = \bar{\bar{R}}_k + \bar{\bar{R}}_k^t = -(v_k + v_k^t) \left(\nabla \vec{U}_k + (\nabla \vec{U}_k)^T - \frac{2}{3} \bar{\bar{I}} \nabla \cdot \vec{U}_k \right) + \frac{2}{3} \bar{\bar{I}} k_k \tag{5}$$

$\bar{\bar{I}}$, k_k , v_k , v_k^t are the identity tensor, turbulent kinetic energy of phase k , its viscosity and its turbulent kinematic viscosity, respectively.

Finally, the last governing equation is the one ensuring the conservation of energy. As we are dealing with low vapour quality two-phase flows, the gas is considered to be saturated at all times. Solving the energy equation for the gaseous phase is inconclusive. Therefore, the energy equation is solved only for the liquid phase. Moreover, since the modelled flows are in the bubbly region for both vertical and horizontal channels, the only form of heat transfer from the gaseous phase to the liquid phase is through condensation (Kurul & Podowzki, 1991). Accordingly, the conservation of energy can be written as follows:

$$\begin{aligned}
& \frac{\partial ((1 - \alpha) i_l)}{\partial t} + \nabla \cdot ((1 - \alpha) i_l \vec{U}_l) \\
& = -\frac{1}{\rho_l} \nabla \cdot [(1 - \alpha) (\vec{q}_l + \vec{q}_l^t)] + \frac{(1 - \alpha)}{\rho_l} \frac{Dp}{Dt} \\
& + \frac{\Gamma_{lg} i_{g,sat} - \Gamma_{gl} i_l}{\rho_l} + \frac{q_w'' A_w'''}{\rho_l}
\end{aligned} \tag{7}$$

This equation is expressed in terms of the specific enthalpy. \vec{q}_l and \vec{q}_l^t are the molecular and turbulent heat fluxes in the liquid phase. The third term represents the phase change per unit volume and the last term corresponds to the heat per unit volume. q_w'' is the heat flux at the wall and A_w''' is the contact area between the wall and the liquid.

3.2 Interfacial Forces

The interfacial forces term in equation (4) represents the forces acting on the bubbles by the surrounding liquid. This term can be split into the following expression:

$$\vec{M}_g = \vec{M}_g^D + \vec{M}_g^L + \vec{M}_g^{WL} + \vec{M}_g^{TD} + \vec{M}_g^{VM} \quad (8)$$

Each of these forces is modelled by a separate model.

3.2.1 Drag Force

\vec{M}_g^D is the drag force. It is the resistance opposed to the bubbles motion in the liquid. The drag is a function of the bubble size and drag coefficient (C_D) (equation (9)). In this study the Schiller Neuman drag model is used for calculating C_D (Schiller & Naumann, 1935). This model is used for dispersed bubbly flows. It calculates C_D based on the bubble Reynolds number (equation (11)) as shown in equation (10).

$$\vec{M}_g^D = -\frac{3}{4} \frac{C_D}{D_b} \rho_l \alpha \|\vec{U}_g - \vec{U}_l\| (\vec{U}_g - \vec{U}_l) \quad (9)$$

$$C_D = \begin{cases} 24(1 + 0.15Re_b^{0.687})/Re_b, & Re_b \leq 1000 \\ 0.44, & Re_b > 1000 \end{cases} \quad (10)$$

$$Re_b = \frac{\rho_l \|\vec{U}_g - \vec{U}_l\| D_S}{\mu_m} \quad (11)$$

$$\mu_m = \alpha_l \mu_l + \alpha_g \mu_g \quad (12)$$

Where μ_m is the mixture dynamic viscosity and D_S is the Sauter diameter.

3.2.2 Lift Force

\vec{M}_g^L is the lift force. Its direction is perpendicular to the drag force. Bubbles move with the flow direction; the drag force will be opposed to the flow direction and the lift force will be in the radial direction. Hence, the lift force plays a role in the radial void fraction distribution in the channel. This force was represented by Drew and Lahey (1987) such as:

$$\vec{M}_g^L = C_L \rho_l \alpha (\vec{U}_g - \vec{U}_l) \wedge (\nabla \wedge \vec{U}_l) \quad (13)$$

To calculate the lift coefficient C_L , the Tomiyama model is employed [eq needs to be fixed look at openfoam code] (Tomiyama et al., 2002).

$$C_L = \begin{cases} \min [0.288 \tanh(0.121 Re_b), f(Eo)], & Eo < 4 \\ f(Eo), & 4 \leq Eo \leq 10.7 \\ -0.288, & Eo > 10.7 \end{cases} \quad (14)$$

$$f(Eo) = 0.0010422 Eo^3 - 0.0159 Eo^2 - 0.204 Eo - 0.474 \quad (15)$$

Where Eo is the Eötvös number (equivalent to the bond number Bo) which is the ratio of the gravitational forces to the surface tension.

$$Eo = Bo = \frac{\Delta \rho g D_s}{\sigma} \quad (16)$$

Where $\Delta \rho$ is the difference between the two phases' densities and σ is the surface tension.

3.2.3 Wall Lubrication

\vec{M}_g^{WL} is the wall lubrication force. It is the force responsible for pushing the bubble away from the wall. This force is best modelled by Antal et al. (1991) as follows:

$$\vec{M}_g^{WL} = \frac{1}{2} C_{WL} \rho_l \alpha D_b \left(\frac{1}{x^2} - \frac{1}{(D-x)^2} \right) \|(\vec{U}_g - \vec{U}_l) \cdot \vec{y}\|^2 \vec{n}_r \quad (17)$$

Where D , x , \vec{y} and \vec{n}_r are the channel diameter, distance from the wall, axial direction and the normal to the wall to the inside of the channel, respectively.

In this study the wall lubrication coefficient C_{WL} is kept as the default value set by OpenFOAM version 7.

3.2.4 Turbulent Dispersion Force

\vec{M}_g^{TD} is the turbulent dispersion force. This force acts on the gas bubbles and is caused by the liquid velocity fluctuations due to turbulence. Even though this thesis looks into the turbulence effect on the void fraction, this force will not be investigated. The Burns model (Burns et al., 2004) is able to cover a large range of flows without any adjustments.

$$\vec{M}_g^{TD} = -\frac{3}{4} C_D \frac{\bar{\alpha}_l \rho_g}{D_s} |\vec{U}_l - \vec{U}_g| \frac{v_g^t}{\sigma} \left(\frac{1}{\bar{\alpha}_g} + \frac{1}{\bar{\alpha}_l} \right) \nabla \bar{\alpha}_g \quad (17)$$

3.2.5 Virtual Mass Force

\vec{M}_g^{VM} is the virtual mass force. It is due to the difference in acceleration between the two phases. A constant virtual mass coefficient of 0.5 is assigned (C_{VM}) for the calculation of the virtual mass force. The effect of this force can be neglected when calculations are run to the point where they reach a steady state.

3.3 Phase Change Model

3.3.1 Boiling Model

The main reason for phase change in the cases studied here is the boiling phenomenon at the heated wall. The wall heat flux can be partitioned into three components:

$$q''_w = q''_c + q''_q + q''_e \quad (18)$$

where q''_c , q''_q and q''_e correspond to the heat flux due to single-phase convection, quenching and vaporization. These three components are expressed in terms of quantities which are calculated in partial steps of the solving procedure.

$$q''_c = (1 - A''')h_c(T_w - T_L) \quad (19)$$

$$q''_q = A''_w h_q(T_w - T_L) \quad (20)$$

$$q''_e = \dot{m}_g H_{LG} \quad (21)$$

where h_c is the convection heat transfer coefficient, h_q is the quenching heat transfer coefficient, T_w is the wall temperature, T_L is the liquid temperature, \dot{m}_g is the generated vapour mass and H_{LG} is the specific mixture enthalpy.

3.3.2 Phase Change Model A

The stated governing equations in section 3.1 consider vaporization and condensation. The rate of vaporization and condensation are denoted by Γ_{gl} and Γ_{lg} correspondingly. In the case of model A, the only phase change possible is near the heated wall because the model only takes into account the mass transfer caused by boiling. Consequently, the condensation rate is always going to be zero and the vaporization rate is calculated as follows:

$$\Gamma_{gl} = \frac{q''_e}{i_{g,sat} - i_l} A''_w \quad (22)$$

3.3.3 Phase Change Model B

The phase change model B considers the phase change happening due to vaporization and condensation at all sections of the modelled geometry. As the bubble detaches from the wall and moves towards the middle of the pipe where the liquid is below saturation temperature, it can condensate back to liquid. This condensation rate is calculated using the following expression:

$$\Gamma_{lg} = \frac{h_{li}(T_{sat} - T_l)a_i}{i_{fg}} \quad (23)$$

where a_i is the interfacial area concentration, which is the area of the gas bubbles per unit, and i_{fg} is the heat transfer coefficient for condensation at the phase interface.

3.3.4 Bubble Diameter

The bubble diameter plays a role in determining the interfacial area concentration, the Sauter diameter and the mass of the generated vapour. The bubble diameter is calculated using an isothermal model that changes with pressure.

$$d_b = d_0 \left(\frac{p_0}{p} \right)^{\frac{1}{3}} \quad (24)$$

where d_b is the mean bubble diameter at p , and d_0 is the bubble diameter at p_0 which is a reference pressure.

3.4 Turbulence Model

The two-phase modified k-epsilon turbulence model is used throughout this study (Lahey, 2005). It is a reliable turbulence model for Reynolds-averaged two-phase simulations (Lahey, 2005; Morel, 2015; Yao & Morel, 2002). The turbulent kinetic energy and its dissipation are calculated for each phase.

3.4.1 Turbulence Equations for the Liquid Phase

As previously stated, the primary continuous phase in this study is the liquid phase. Therefore, the k-epsilon turbulence model needs to account for the turbulence created by the dispersed phase (the gaseous phase). This is visible in Zaepfell (2012) denotation of the k-epsilon model adapted for the continuous phase of bubbly flows.

$$\begin{aligned}
& \frac{\partial}{\partial t}(\alpha_l \rho_l k_l) + \nabla \cdot (\alpha_l \rho_l k_l \bar{V}_l) \\
& = -\alpha_l \rho_l \bar{\bar{V}}_l : \bar{\bar{V}}_l - \alpha_l \rho_l \varepsilon_l + \nabla \cdot \left(\alpha_l \rho_l \frac{v_l^t}{\sigma_k} \nabla k_l \right) + P_k^I
\end{aligned} \tag{25}$$

$$\begin{aligned}
& \frac{\partial}{\partial t}(\alpha_l \rho_l \varepsilon_l) + \nabla \cdot (\alpha_l \rho_l \varepsilon_l \bar{V}_l) \\
& = -\alpha_l \rho_l C_{\varepsilon 1} \frac{\varepsilon_l}{k_l} \bar{\bar{V}}_l : \bar{\bar{V}}_l - C_{\varepsilon 2} \alpha_l \rho_l \frac{\varepsilon_l^2}{k_l} + \nabla \cdot \left(\alpha_l \rho_l \frac{v_l^t}{\sigma_\varepsilon} \nabla \varepsilon_l \right) \\
& + P_\varepsilon^I
\end{aligned} \tag{26}$$

where k_l is the turbulent kinetic energy in the liquid, ε_l is the dissipation of the turbulent kinetic energy in the liquid, \bar{V}_l is the mean liquid velocity and $\bar{\bar{V}}_l$ is the double velocity correlation tensor.

The last terms on the RHS of equations (25) and (26), P_k^I and P_ε^I , corresponds to the interfacial production that result from the turbulence generated in the wake of a bubble. The latter terms can be expressed as:

$$P_k^I = -\bar{M}_g^D \cdot (\bar{V}_g - \bar{V}_l) \tag{27}$$

$$P_\varepsilon^I = C_{\varepsilon 3} \frac{\varepsilon_l}{k_l} P_k^I \tag{28}$$

where \bar{M}_g^D is the drag force per unit volume.

Observing the equations in this section, one can see the existence of a coefficient, $C_{\varepsilon 3}$, that links the turbulence to the bubbles' transport in equation (28). The effect of this coefficient on the radial gas void fraction distribution is studied in section 5.1.3 .

3.4.2 Turbulence Equations for the Gaseous Phase

For the dispersed gaseous phase, similar equations are used with some modifications to account for phase separation. This model considers the gaseous phase to behave like the liquid phase until it reaches a certain void fraction after which the turbulence in the gas is treated the same as the turbulence produced in a single-phase flow.

Chapter 4

Methodology

In this chapter, firstly, a brief overview of the CFD application employed throughout this study is presented. Secondly, the test cases to which the solver is benchmarked are introduced. Lastly, the numerical approach used to model the test cases into OpenFOAM is laid out.

4.1 OpenFOAM

4.1.1 OpenFOAM Brief

The CFD tool of choice for this research project is OpenFOAM version 7. OpenFOAM is a C++ based open-source toolbox. It is able to solve physical problems using both the Finite Element and the Finite Volume method. However, OpenFOAM is mostly known for the latter since it is primarily used for CFD applications. Just like any simulation tool, its usage requires three steps: pre-processing, solving and post-processing as show in Figure 6.

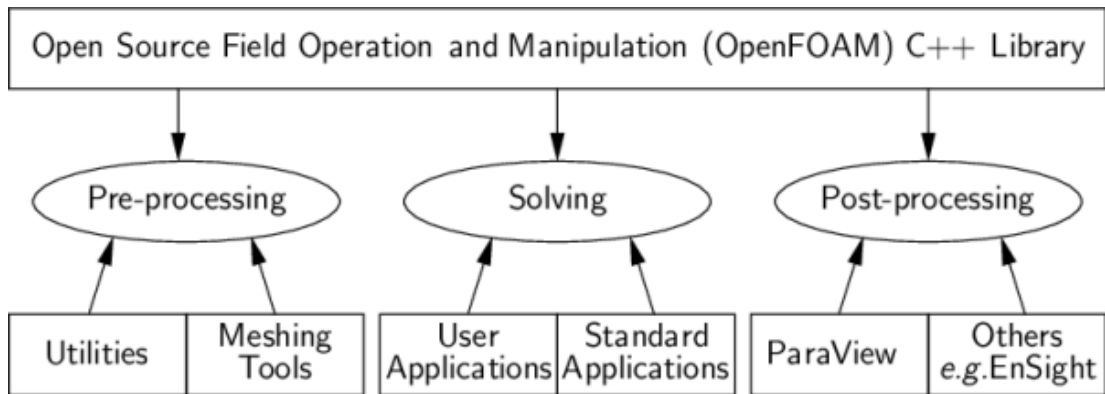


Figure 6 OpenFOAM structural overview

For the pre-processing, blockMesh is used to create and discretize the simulated geometry. It is one of the utilities provided by OpenFOAM. This meshing tool allows full access to the mesh generation process as every mesh detail is described in the dictionary file, blockMeshDict, used to produce the mesh. To run an application in order to solve a case, a simple directory structure specific to OpenFOAM must be followed. Figure 7 presents the three directories that are required in an OpenFOAM case folder. A system directory contains all the dictionary files, in other words all the

files that dictate the parameters related to the solution procedure. A constant directory includes the case mesh and files describing the physical properties. Finally, a time directory, usually named 0, comprises the files necessary to set the initial conditions of the case. The blockMeshDict file previously mentioned falls under the system directory and after it gets compiled using blockMesh, it creates the polyMesh directory that defines the computational grid.

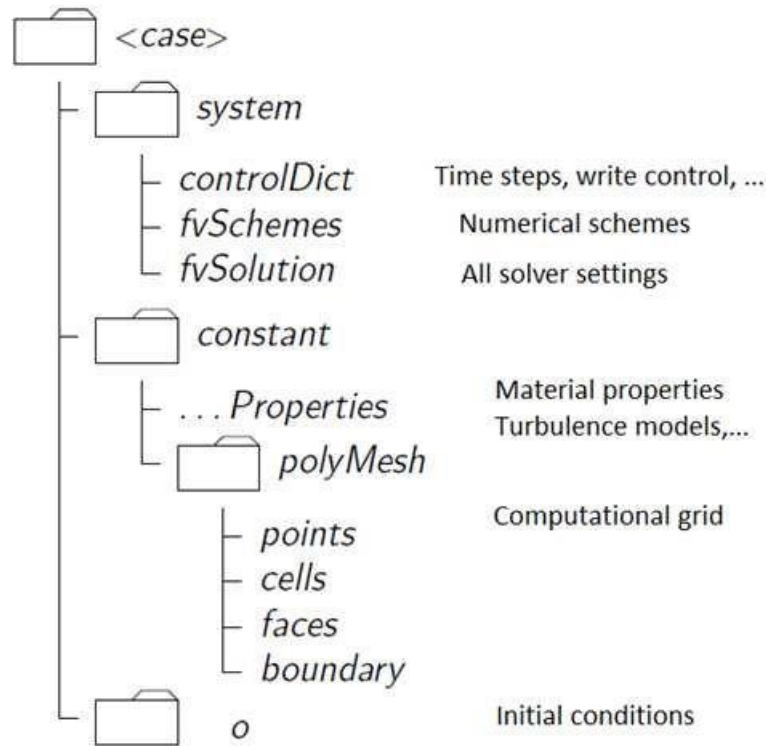


Figure 7 Outline of a basic OpenFOAM directory

4.1.2 Two-Phase Solver

OpenFOAM is equipped with pre-built standard applications also known as solvers. These solvers are usually developed based on published articles of mathematical models. Simulating a boiling flow case necessitates utilizing a solver that entails the mathematical models detailed in Chapter 3. After careful examination of the implemented solvers' codes, reactingTwoPhaseEulerFoam is found to be the most adequate to simulate the evaluated cases in this thesis. It can solve for two compressible fluid phases while accounting for momentum, heat and mass transfer (Cappelli, 2018). However, even if this solver looks like it can simulate boiling flows on paper, it is not enough. The code implementation can contain bugs that might cause

it to malfunction. Therefore, to trust the solver's results a validation based on experimental data must be conducted.

OpenFOAM works best with Linux based operating systems. To be able to use it on Microsoft Windows, an emulator of a Linux machine is needed. The latter has been used in this the case. The studied simulations are run a machine with 2 Intel Xeon(R) W-2155 CPUs @ 3.30 GHz having 10 cores and 20 logical processors.

4.2 Test Cases

4.2.1 DEBORA 6 Experiment

The DEBORA 6 experiment is a boiling flow experiment conducted with R12 on a vertical macro-scale channel. The details of the experiment are mentioned in section 2.1 . The main point of interest is the local radial temperature and void fraction distribution. For DEBORA 6, the initial conditions for the experiment are presented in Table 3.

Table 3 DEBORA 6 experimental conditions

Case	Pressure (<i>bar</i>)	Mass Flux ($\frac{kg}{m^2s}$)	Wall Heat Flux ($\frac{kW}{m^2}$)	Inlet Temperature ($^{\circ}C$)	Saturation Temperature ($^{\circ}C$)	Inlet Vapour Quality
DEB 6	26.15	1984.9	73.89	70.53	86.73	0

R12 flow upwards in the vertical pipe. It has an internal diameter of 19.2 mm and a wall thickness of 2 mm. This thickness is irrelevant as only the internal flow is modelled. The pipe has a 3.5-meter heated section where the heat flux mentioned in Table 3 is applied. The entire channel length is 5 meters. The heated section is 1 meter away from the inlet and 0.5 meters away from the outlet (Figure 8). These separation sections are adiabatic, so the boiling can only take place at the heated section.

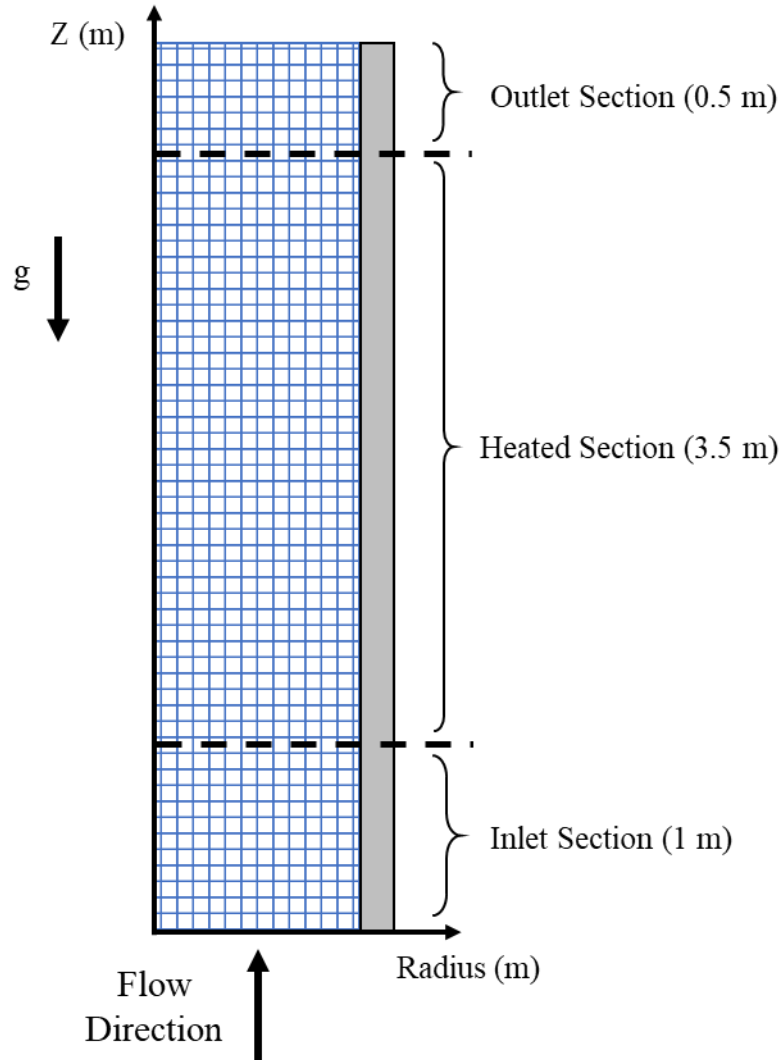


Figure 8 DEBORA 6 pipe configuration

The experimental data is measured with an optical probe located at 4.485 meters from the inlet, hence the experimental data is collected as radial profiles at the position of the probe (Figure 9). The evaluated data in Chapter 5 follows the same scheme, data is extracted over a line at section A-A. DEBORA 6 provides a radial temperature distribution and a radial gas void fraction profile showcased in Appendix A, Figure 40 and Figure 41.

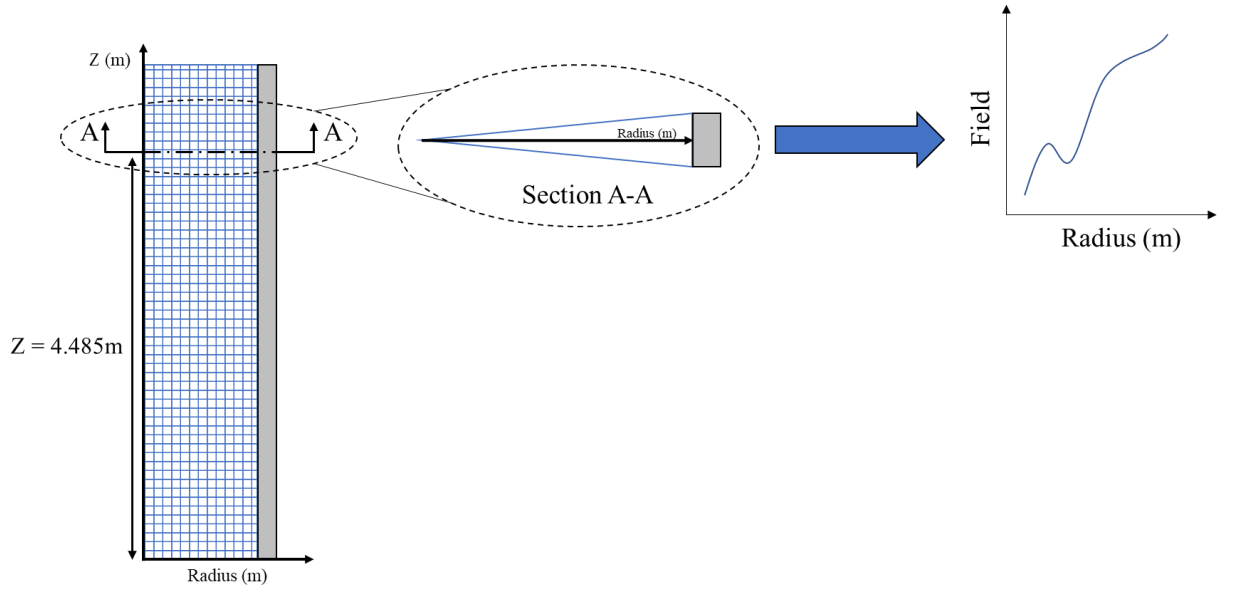


Figure 9 Data extraction layout

4.2.2 CO₂ CERN Experiment

The 2PACL cooling system, just like any other is comprised of a primary and secondary circuit as illustrated in Figure 10. This system transports liquid CO₂ from point 1 to point 3, where the liquid enters micro-channels leading into the detector. As the liquid passes through the detector, it absorbs the heat emitted by the electric circuits and evaporates. Hence the flow from point 5 to point 6 is two-phase. This flow then passes in a condenser where the heat is ejected and the flow condensates back to liquid. It is important to note that two-phase CO₂ passes by both macro-scale and micro-scale channels. The section mimicked by the Hellenschmidt and Petagna (2020) is the evaporator section. This experiment is conducted to help better understand the behaviour of CO₂ in micro-channels in order to eventually aid in the design of the evaporator.

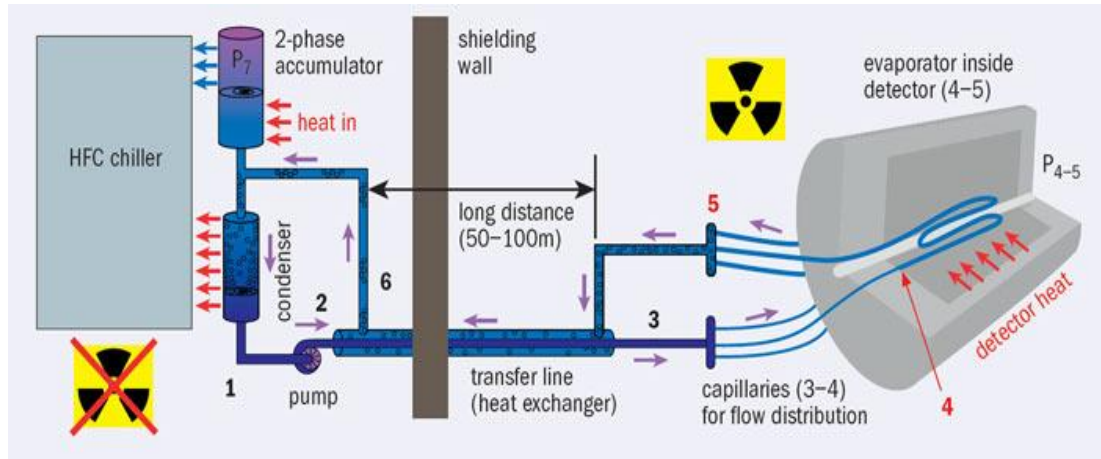


Figure 10 Schematic of CERN/CMS detector cooling system

An experimental setup, displayed in Figure 11, is designed and built with the aim of extracting accurate and precise pressure drop data across a horizontal heated tube section. Three tube diameters are assessed: 2.15 mm, 1 mm, and 0.5 mm. For the current study, the main interest is the 1 mm diameter tube, but one case is tested with the 2.15 mm tube for additional validation. The heated section of the pipe is 170 mm, but the section where the pressure drop is monitored is 200 mm as illustrated in Figure 12. The experimental data presented by Hellenschmidt and Petagna (2020) is displayed in Appendix B, Figure 42. In this experiment, the inlet temperature is equal to the saturation temperature. The test cases chosen for the CO₂ study are noted in Table 4.

Table 4 CO₂ experimental conditions for chosen test cases

Case	Pressure (bar)	Mass Flux ($\frac{kg}{m^2s}$)	Wall Heat Flux ($\frac{kW}{m^2}$)	Tube Inner Diameter (mm)	Saturation Temperature (°C)	Inlet Vapour Quality
1	50.871	800	10	1	15	0
2	50.871	800	20	1	15	0
3	50.871	800	30	1	15	0
4	50.871	400	10	1	15	0
5	50.871	460	10	1	15	0
6	50.871	400	10	2.15	15	0

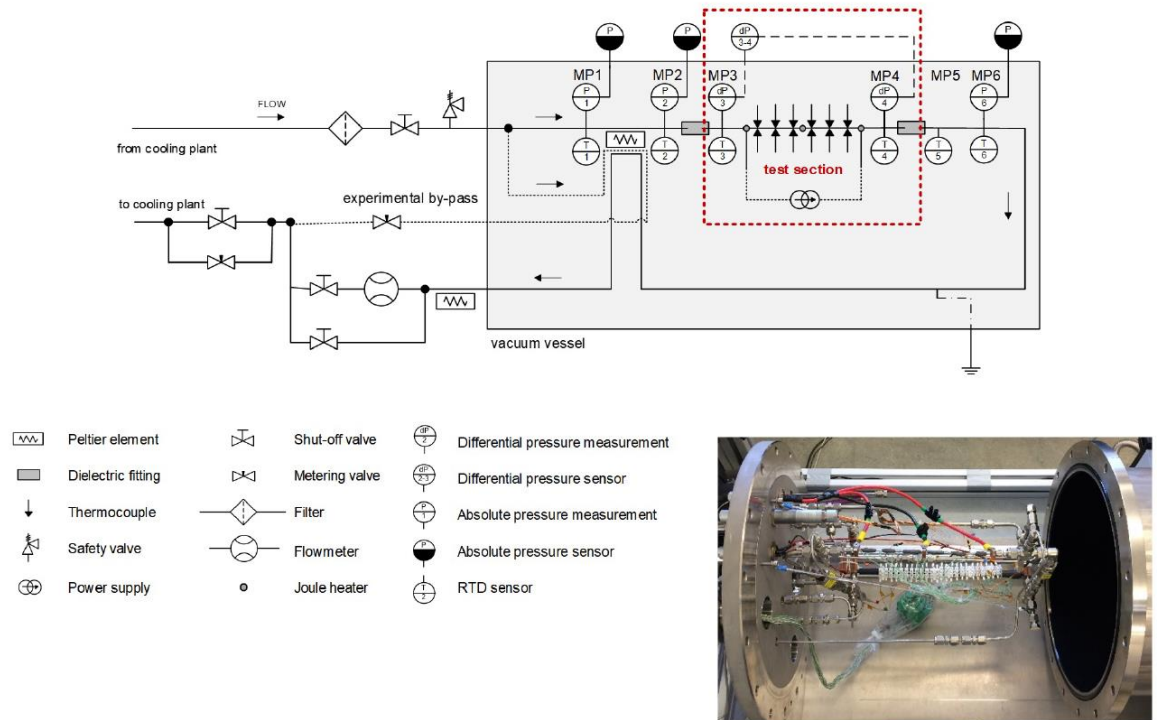


Figure 11 CERN experimental setup

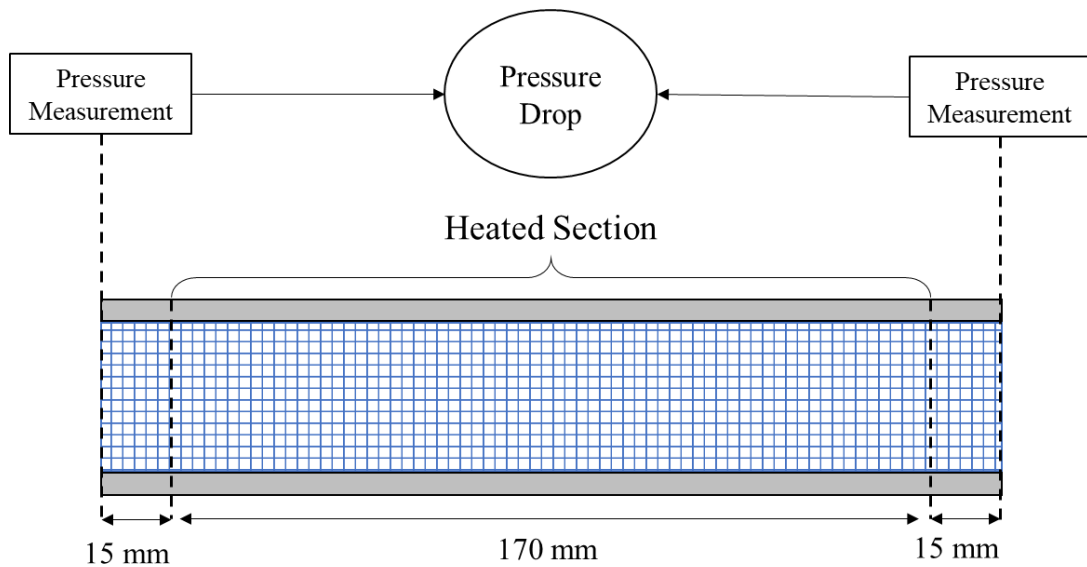


Figure 12 Pressure drop section schematic

4.3 Numerical Approach

4.3.1 R12 Simulations

4.3.1.1 Geometry

The vertical pipe for the R12 simulations is modelled as an axisymmetric wedge (Figure 13). This configuration is possible because of the direction of the pipe.

Here, the gravity force acts in the negative axial direction therefore making the symmetry assumption possible.

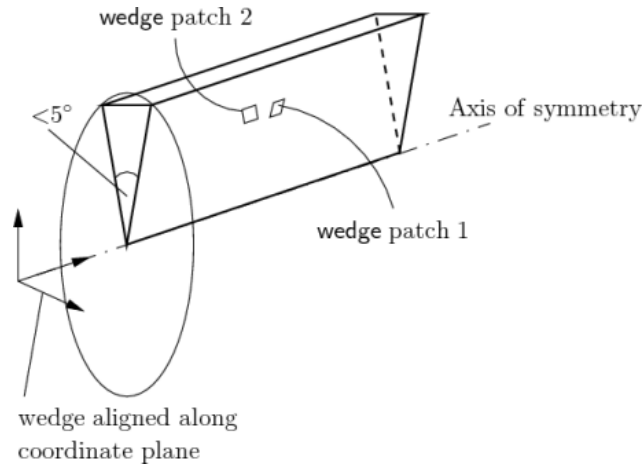


Figure 13 2D-axisymmetric wedge

The wedge angle considered is 5 degrees, which is the recommended value for this type of modelling. The geometry is recreated to match what is shown in Figure 8. Having inlet and outlet sections is important to extract results independent from the boundary conditions set at the inlet and outlet.

4.3.1.2 Mesh Generation

As per the blockMeshDict file, the mesh elements are defined in the directions x_1 , x_2 and x_3 as illustrated in Figure 14.

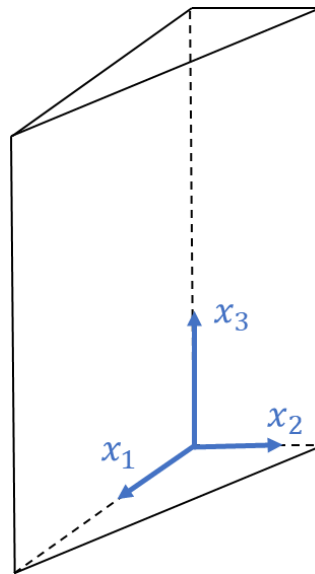


Figure 14 Direction of mesh vectors for the R12 wedge geometry

Three different meshes are evaluated in Chapter 5. They are denoted as coarse mesh, medium mesh and fine mesh. The elements of each mesh are detailed in Table 5. An example of the medium mesh at the cross section and face of the wedge is displayed in Figure 15 and Figure 16, respectively.

Table 5 Mesh element configurations for the R12 simulations

Mesh	x_1	x_2	x_3	Number of Cells
Coarse	10	1	1000	10000
Medium	25	1	560	14000
Fine	20	1	1000	20000



Figure 15 Mesh cross section for the R12 medium mesh

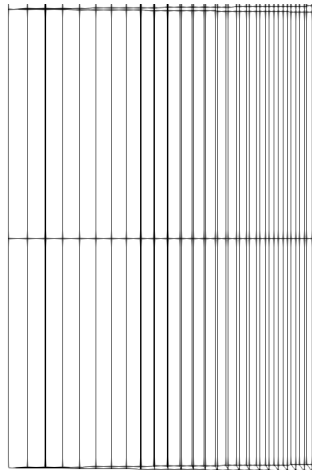


Figure 16 Axial view of the medium mesh

4.3.1.3 Boundary Conditions

For the R12 simulations, one set of boundary conditions is needed. The inlet for the simulation is set as a velocity inlet, the outlet as a pressure outlet, the inlet temperature and heat flux are set according to Table 3. The inlet velocity is calculated by dividing the mass flux of the inlet liquid flow with the liquid density at the inlet. At the inlet, the density of R12 is equal to 1127 kg/m³. This density will only be used for the calculation of the inlet velocity.

$$V_{in}^{R12} = \frac{\text{Experimental Mass Flux}}{\rho_{in}^{R12} \text{ for R12}} = \frac{1984.9}{1127} = 1.76 \frac{m}{s} \quad (29)$$

Hence the Reynolds number for this simulation is calculated as:

$$Re_{R12} = \frac{\rho_{in}^{R12} V_{in}^{R12} D}{\mu_{in}^{R12}} = \frac{1127 \times 1.76 \times 19.2 \times 10^{-3}}{116.53 \times 10^{-6}} = 326814 > 4000 \quad (30)$$

The Reynolds will be calculated internally by the solver, this is only to check if the flow is turbulent and indeed it is.

As for the liquid and gas properties, they are taken at the saturation temperature $T_{sat} = 86.73$ °C. This can be proved by examining the experimental temperature distribution which hovers around the saturation temperature. The required properties are found in Table 6.

Table 6 Thermophysical properties for the R12 simulations

Phase	Temperature (°C)	Pressure (bar)	Density ($\frac{kg}{m^3}$)	Enthalpy ($\frac{kJ}{kg}$)	C _p ($\frac{kJ}{kg \cdot K}$)	Molar Mass	Viscosity ($\mu Pa \cdot s$)	Prandtl	Surface tension (mN/m)
Liquid	86.73	26.15	1017.1	292.53	1.4198	120.91	89.5	2.78	1.77
Gas	86.73	26.15	172.05	378.60	1.2907	120.91	16.4	1.19	1.77

4.3.2 CO₂ Simulations

4.3.2.1 Geometry

For the CO₂ simulations, an axisymmetric representation of the geometry is not possible because gravity is in the radial direction and the pipe is horizontal. Additionally, it cannot be modelled as a 2D planar geometry since in 2D the buoyancy effect is not captured. Therefore, a 3D pipe must be modelled. This pipe will be

modelled as a cylinder that corresponds to the volume of fluid in the pipe. The geometry is split into an inlet, heated and outlet section (Figure 17) similar to the concept used for the R12 simulations.

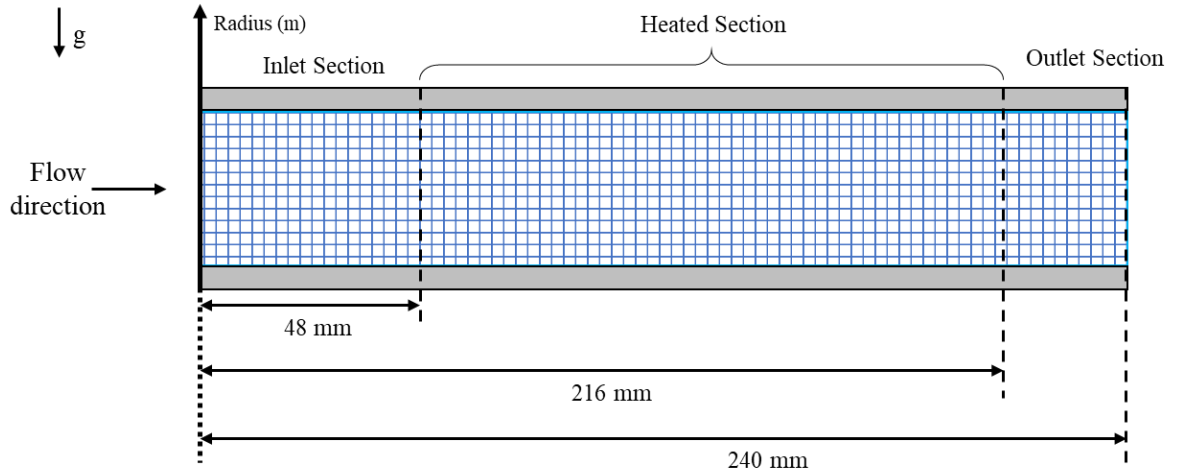


Figure 17 Initial geometry for the CO₂ simulations

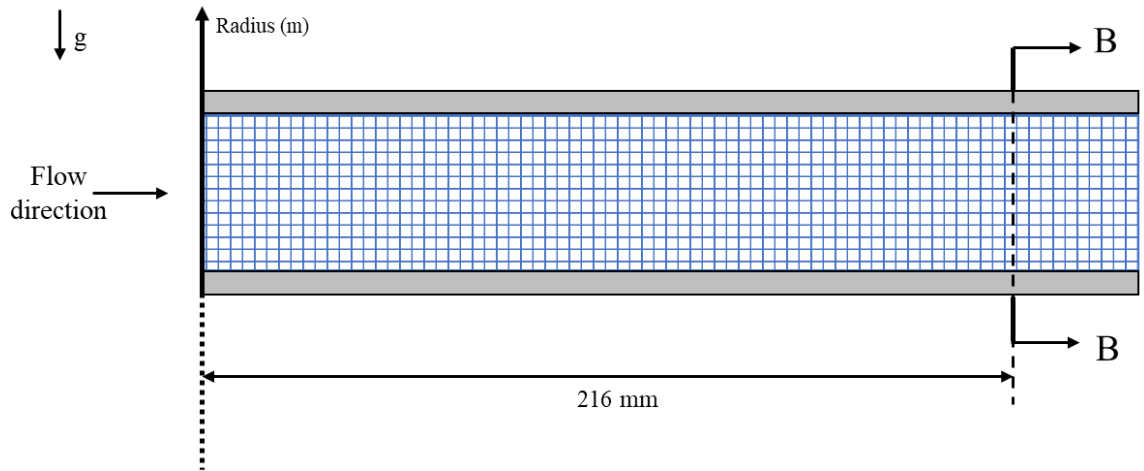


Figure 18 Section for CO₂ data extraction (initial geometry)

The data in Figure 19 is plotted over section B-B (Figure 18)

To prove that a 2D planar geometry cannot represent the actual physics of the case, Figure 19 shows the radial void fraction for both a 2D and 3D simulation at section B-B from Figure 18. The gas void fraction in the 2D case is thicker near the bottom part of the pipe (from 0 to 0.0002 meters), on the other hand the thick gas film in the 3D simulation is at the top part that is resulting from the migration of the gas formed near the wall around the pipe to the top section following the yellow arrows. In the 2D

planar geometry, this is not possible because there is nothing connecting the bottom wall of the channel to the top wall.

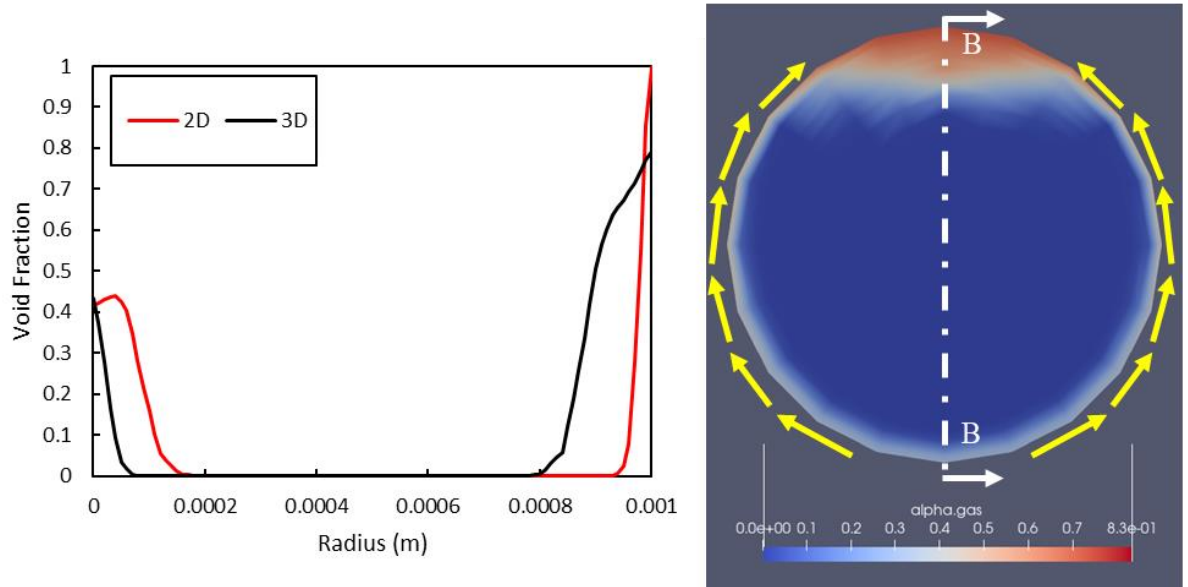


Figure 19 2D vs 3D for CO_2 simulations

Initially the length of the modelled channel is 0.24 meters; however, in Chapter 5, this length is not enough to ensure an adequate flow mixing. Hence, a longer pipe of length 0.5 meters is modelled. Figure 20 shows the sections over which the pressure drops are assessed in Chapter 5 and Figure 21 outlines sections B-B and C-C where the CO_2 data is extracted for the discussions.

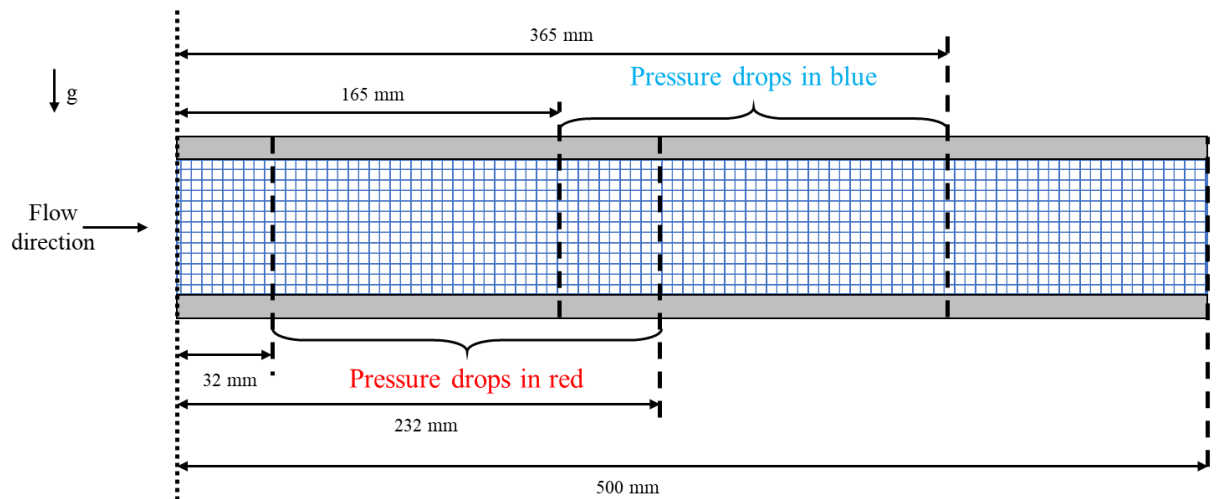


Figure 20 CO_2 simulations modified geometry

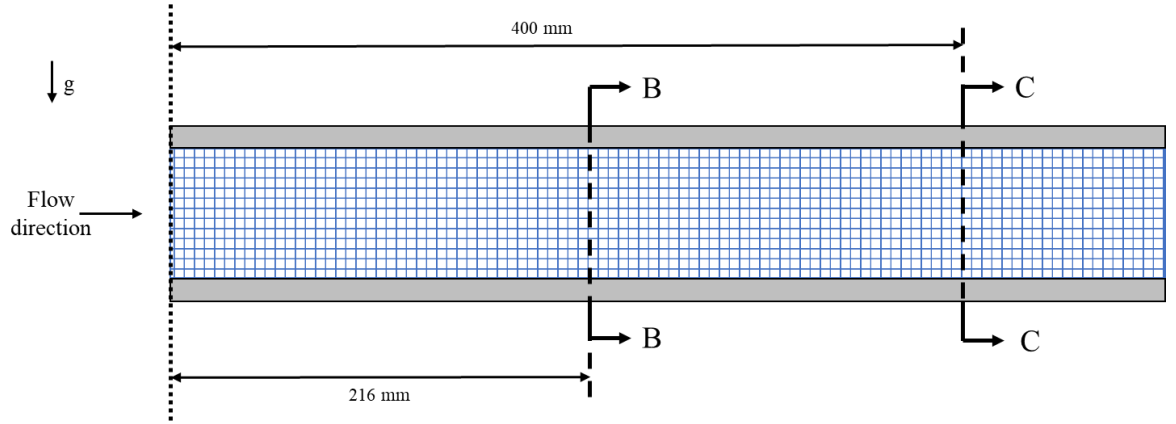


Figure 21 Data extraction sections from the CO_2 simulations

4.3.2.2 Mesh Generation

For this 3D cylindrical geometry, the mesh is an O-type structured mesh. This structure splits the geometry into 2 main blocks. The inner block which is a rectangular cuboid, and the outer block is a cylinder out of which the cuboid is subtracted. This structure allows us to have a mesh of hexahedron elements as displayed in Figure 22.

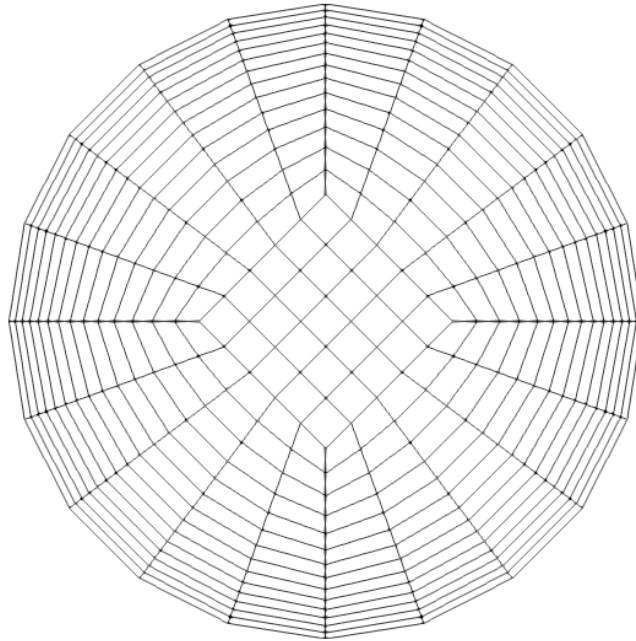


Figure 22 CO_2 O-type mesh structure

Similarly, to the R12 simulations, three different meshes are evaluated referred to as coarse mesh, medium mesh and fine mesh. Figure 23 shows the direction in which the

vector for element definition is taken. Table 7 shows the difference between the three meshes taking into consideration these vector directions.

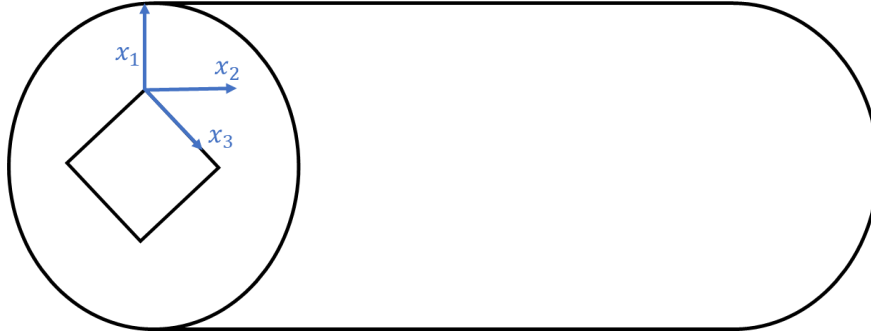


Figure 23 Direction of mesh vectors for the CO₂ cylindrical geometry

Table 7 Mesh element configurations for the CO₂ simulations

Mesh	x_1	x_2	x_3	Number of Cells
Coarse	5	75	5	9375
Medium	10	60	5	13500
Fine	14	60	5	18300

4.3.2.3 Boundary Conditions

Boundary conditions for the CO₂ simulations are in line with the conditions mentioned in Table 4. The velocity is calculated from the mass flux using equation (29) but the density is evaluated at the saturation temperature. In Fact, All the properties are evaluated at saturation temperature (Table 8). The maximum Reynolds number for these simulations is 11405, which corresponds to a low Reynolds number flow.

Table 8 Thermophysical properties for the CO₂ simulations

Phase	Temperature (°C)	Pressure (bar)	Density ($\frac{kg}{m^3}$)	Enthalpy ($\frac{kJ}{kg}$)	C _p ($\frac{kJ}{kg.K}$)	Molar Mass	Viscosity ($\mu Pa.s$)	Prandtl	Surface tension (mN/m)
Liquid	15	50.871	821.21	239.99	3.4360	44.01	74.433	2.78	1.95
Gas	15	80.871	160.73	416.64	3.2371	44.01	16.952	1.96	1.95

Chapter 5

Results and Discussion

In this chapter, the results for the simulations are discussed. Starting with the macro-scale vertical channel with R12 flow and then moving on to the micro-scale horizontal channel with CO₂ flow.

5.1 R12 Results

5.1.1 Time and Mesh Sensitivity Analysis

The first step in any transient CFD simulation establishing results which are time step and mesh independent.

The time step for both R12 and CO₂ simulations is adaptive. This adaptive time step is a function of the Maximum Courant Number. For all simulations in this study, the maximum Courant Number does not exceed 0.7 (equation (31)). The time step is always changing to guarantee the previously mentioned condition. This ensures that information is propagating through one mesh cell at each time step. Additionally, it helps with stabilizing the simulation.

$$C_{max} = \frac{u\Delta t}{\Delta x} \leq 0.7 \quad (31)$$

where u , Δt and Δx are the velocity magnitude in a grid element, the time step, and the length interval of the element, respectively.

The mesh plays an important role in having accurate results. Mesh optimization is one of the most delicate tasks when running a CFD simulation because there is always a trade-off that one needs to consider. A fine mesh can capture the most details, but it will take very long in simulation runtime. A coarse mesh will run faster yet the results might not capture all the flow characteristics. Ideally, the best mesh is one that balances this trade-off. For the R12 simulations, the void fraction, as represented in equation (32), and temperature are the parameters of interest; therefore, the mesh independence study is conducted on the latter two.

$$\alpha = \frac{V_g}{V_g + V_l} \quad (32)$$

where α is the fraction of the cell volume that is occupied by the gaseous phase, hence V_g is the gas filled volume and V_l is the liquid filled volume.

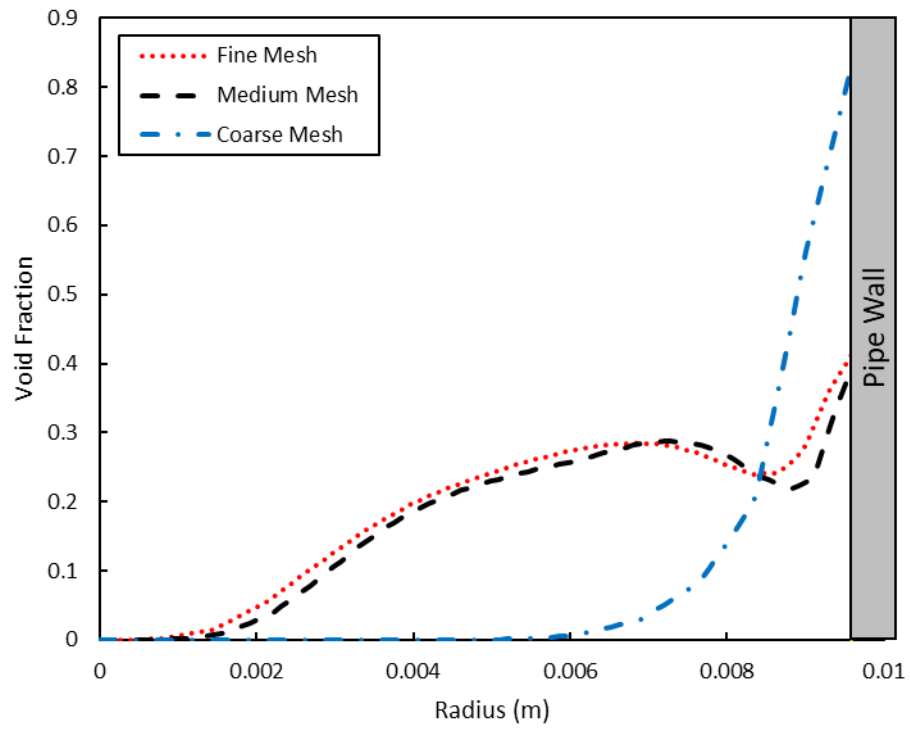


Figure 24 Void Fraction mesh sensitivity analysis for the R12 simulations

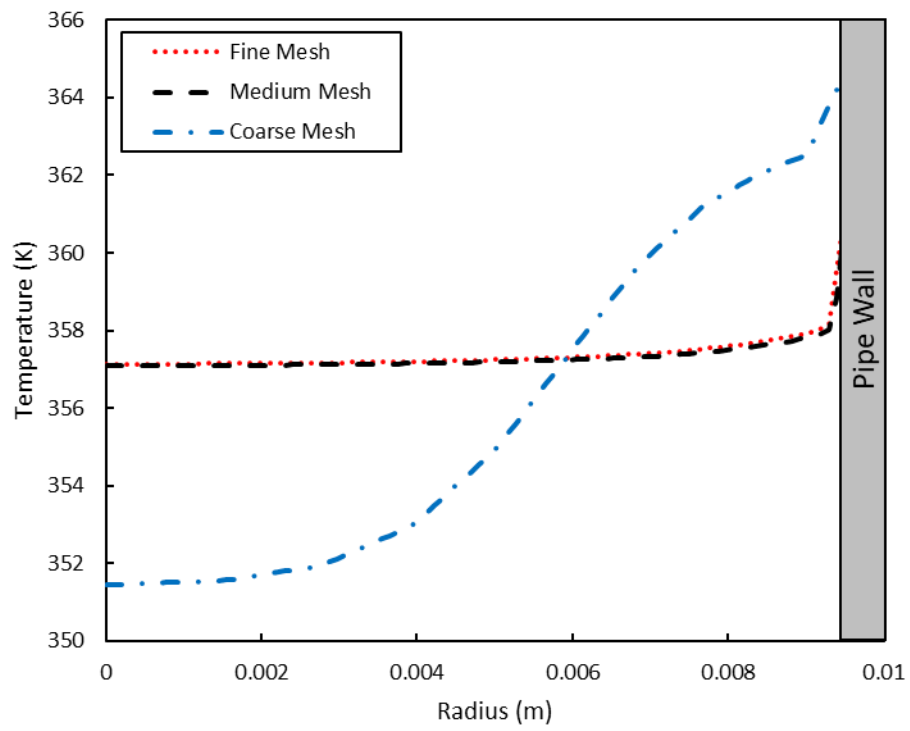


Figure 25 Temperature mesh sensitivity analysis for the R12 simulations

Figure 24 and Figure 25 illustrate the radial void fraction plots and the radial temperature distribution, respectively, both at 4.485 meters from the inlet. It is obvious that the results of the simulation with the coarse mesh diverge from those of the medium and fine mesh. On the other hand, the results with the medium mesh show a noticeable agreement with the ones of the fine mesh. The maximum absolute error (AE as presented in Appendix C equation (33)) in void fraction between both meshes is 0.07 and the maximum absolute error in temperature is 0.71 K; these errors are considered negligible. The runtime with the fine mesh is significantly longer; it increases the simulation runtime by 120 hours when compared to the runtime with the medium mesh. Based on the above-stated, the medium mesh is selected for the R12 simulations.

As the appropriate mesh is decided, a further validation will be conducted to show the ability of reactingTwoPhaseEulerFoam in modelling boiling flows.

5.1.2 $C_{\varepsilon 3}$ Sensitivity Analysis

In section 4.3.1.3, the details of the geometry and boundary conditions of the DEBORA 6 experiment are noted (Garnier et al., 2001). This experiment is the basis of the R12 simulation validation. As part of this validation, $C_{\varepsilon 3}$, the coefficient detailed in section 3.4.1, is varied. Five different values of $C_{\varepsilon 3}$ are evaluated: 0, 0.1, 1, 1.3 and 1.5.

Comparing the numerical results with the experimental data represented in a black dashed line in Figure 26, $C_{\varepsilon 3}$ equals 1.3 and 1.5 are immediately eliminated. They yield a high root relative squared error (RRSE as presented in Appendix C equation (34)); $C_{\varepsilon 3}$ equals 1.3 presents an error of 80% and $C_{\varepsilon 3}$ equals 1.5 an error of 82%. $C_{\varepsilon 3}$ equals 0 and 0.1 show a RRSE of 40%, which is a good improvement on the $C_{\varepsilon 3}$ equals 1.3 and 1.5. The best results are captured with $C_{\varepsilon 3}$ equals 1, yielding a RRSE of 34% and a maximum absolute error of 0.21 as depicted in Figure 27.

Having observed the behaviour of the above mentioned flows, one can say that the gas void fraction distribution for $C_{\varepsilon 3}$ equals 0 is similar to that of $C_{\varepsilon 3}$ equal 0.1 and the distribution for $C_{\varepsilon 3}$ equal 1.3 is similar to that of $C_{\varepsilon 3}$ equal 1.5. $C_{\varepsilon 3}$ equals 1 looks in trend similar to $C_{\varepsilon 3}$ equal 0 and 0.1 but it is different in terms of gas void fraction

magnitudes. Therefore, for further flow assessment, the turbulence parameters for $C_{\varepsilon 3}$ equals 0.1, 1 and 1.5 are analysed and discussed.

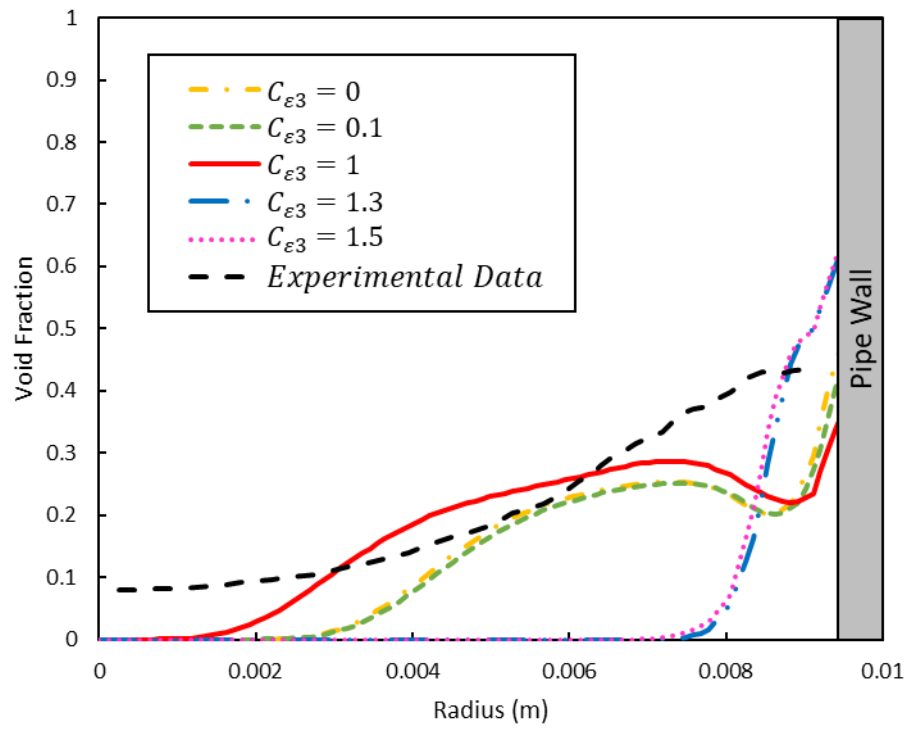


Figure 26 Effect of $C_{\varepsilon 3}$ on the void fraction distribution in the R12 simulations

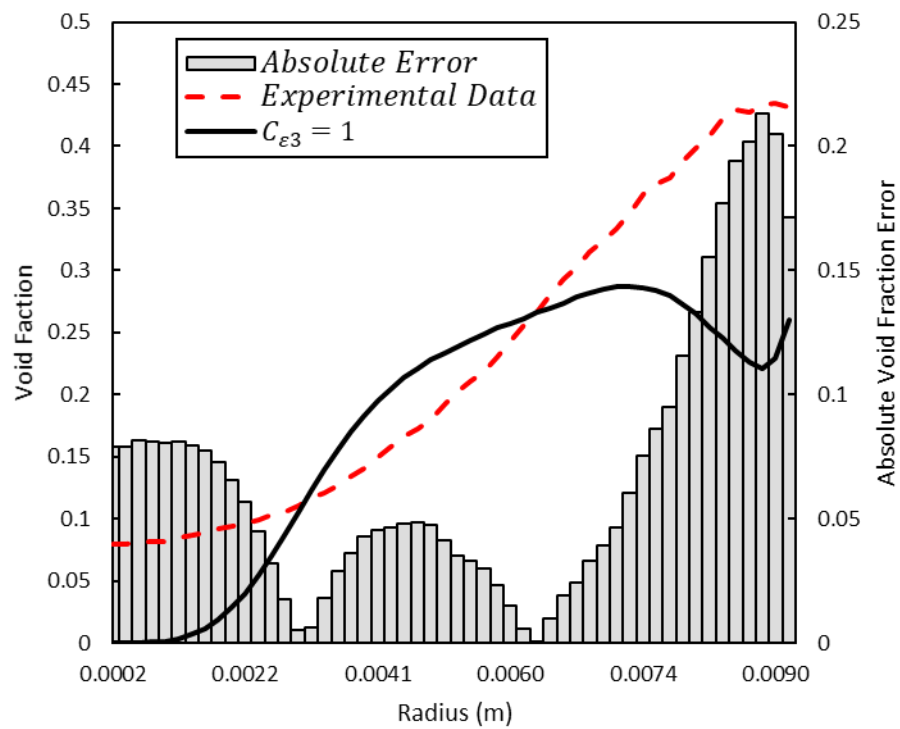


Figure 27 Comparison of numerical void fraction results and experimental data

5.1.3 Turbulence Quantities Assessment

The $C_{\varepsilon 3}$ sensitivity analysis proved that the flow turbulence plays an important role in the phase change and gas void fraction distribution in a boiling flow. Here the turbulent kinetic energy (k) and the dissipation of the turbulent kinetic energy (ε) for the liquid phase and gaseous phase are studied at a section located at 4.485 meters from the inlet.

In Figure 28, the left axis represents both the gas void fraction and the turbulent kinetic energy while the right axis corresponds to the dissipation of the turbulent kinetic energy. The different gas void fraction distribution can be attributed to the two turbulence parameters. As shown by Figure 28, (c) an underestimation in the liquid turbulence dissipation leads to an overestimation in the effect of convection at the wall. As a result, the gas void fraction is over predicted. In both (a) and (b), the liquid turbulence dissipation near the wall is lower hence the gas void fraction is less. In the latter two, phase change near the wall is reduced because of the reduction of convection. It is the balance between the turbulent kinetic energy in the liquid and its dissipation that dictate the phase change at the wall. When turbulence is produced and not dissipated, heat transfer is enhanced and consequently more gas is produced at the heated wall. Moreover, the transportation of gas void fraction across the channel radius is governed by the turbulent kinetic energy in the liquid; this can be clear when looking at (a), (b) and (c). In (c), the gas void fraction does not propagate into the middle of the pipe, this is linked to the near zero turbulent kinetic energy from 0 to 0.008 meters. In contrast, in (a) and (b), the gas void fraction dissipates away from the pipe wall to the midsection. The higher the turbulent kinetic energy farther from the wall, the higher the gas void fraction. The gas void fraction in (b) from 0 to 0.008 meters is bigger in magnitude than that in (a), correspondingly the turbulent kinetic energy in (b) in the channel midsection is higher than that in (a). The difference in gas void fraction near the wall in both (a) and (b) is attributed to the balance between the turbulent kinetic energy in the liquid and its dissipation.

Figure 28 (d), (e) and (f) display the turbulent kinetic energy and its dissipation in the gas. When discussing the turbulence quantities of the gas, it is necessary to note that the gas here is a discrete phase. The turbulence in the gas does not play an important role in the transportation and dissipation of gas into the pipe.

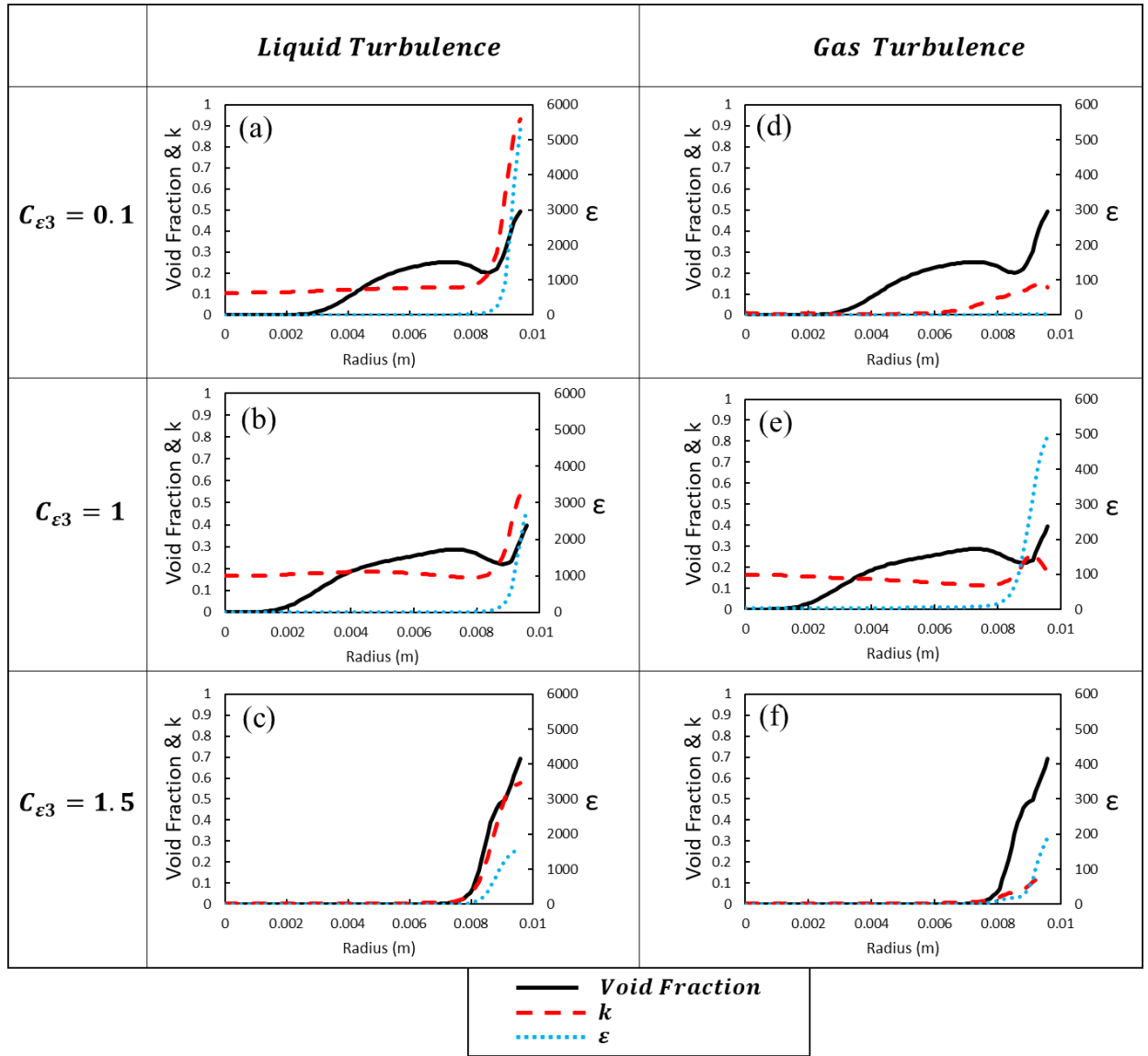


Figure 28 Liquid and gas turbulence comparison in R12 simulations

In light of this discussion, it is evident that the turbulence quantities of the liquid are what govern the boiling near the heated wall and the diffusion of the gas far from the wall. The near wall phase change is directly related to the dissipation of the turbulent kinetic energy of the liquid while the dissipation of the gas into the middle of the channel is directly linked to the liquid turbulent kinetic energy of the liquid itself.

reactingTwoPhaseEulerFoam has two phase change models. These models are described in section 3.3 . For all of the previously shown simulations, phase change model A is used, where only the phase change due to boiling is accounted for. In Figure 29, model B is evaluated.

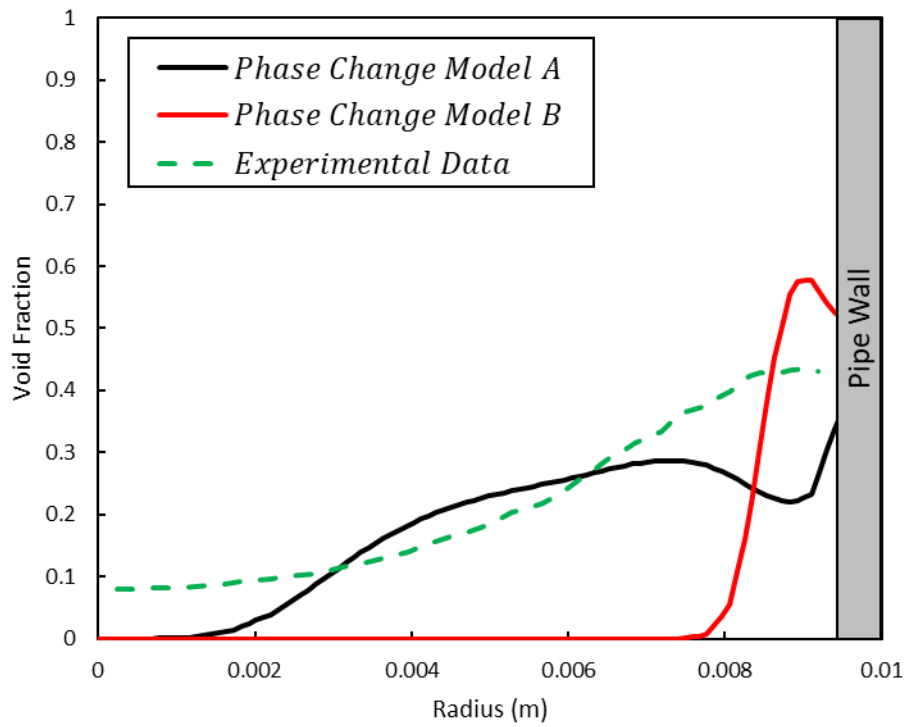


Figure 29 Comparison of reactingTwoPhaseEulerFoam phase change models

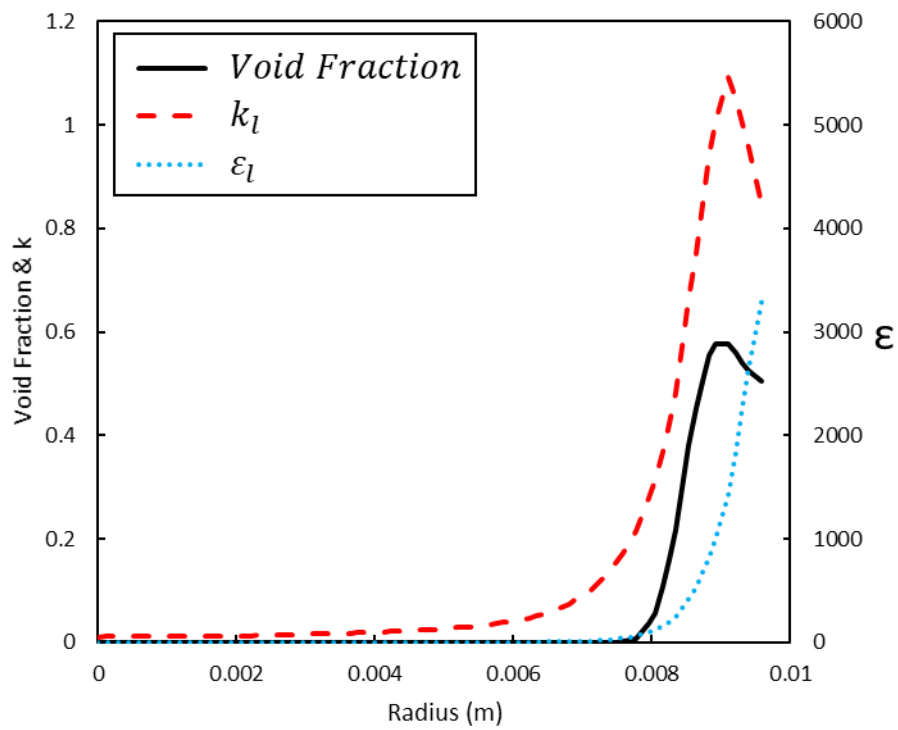


Figure 30 liquid turbulence results for the liquid phase change model B

Figure 29 clearly shows that phase change model **A** is better at predicting the gas void fraction distribution. As a sanity check, all the previously evaluated $C_{\varepsilon 3}$ values are tested with Model **B** and in all the cases, model **A** outperforms model **B**. To further enforce the previous conclusion, Figure 30 presents the turbulence quantities of the liquid when using model **B**. As expected, the dissipation of the turbulent kinetic energy in the liquid is small near the wall compared to Figure 28 (a) thus promoting an overestimation of the gas void fraction. On the other hand, the turbulent kinetic energy is near zero towards the middle of the pipe which explains why there is no dissipation of gas towards the midsection of the channel. Model **A** works best in this particular case because this is a low vapour quality flow with a relatively low heat flux.

In the above discussion, the gas void fraction is the only parameter being analyzed. Another significant property is the liquid temperature. In all the achieved simulations, the discrepancy in the predicted temperature field and the DEBORA 6 experimental data is relatively high.

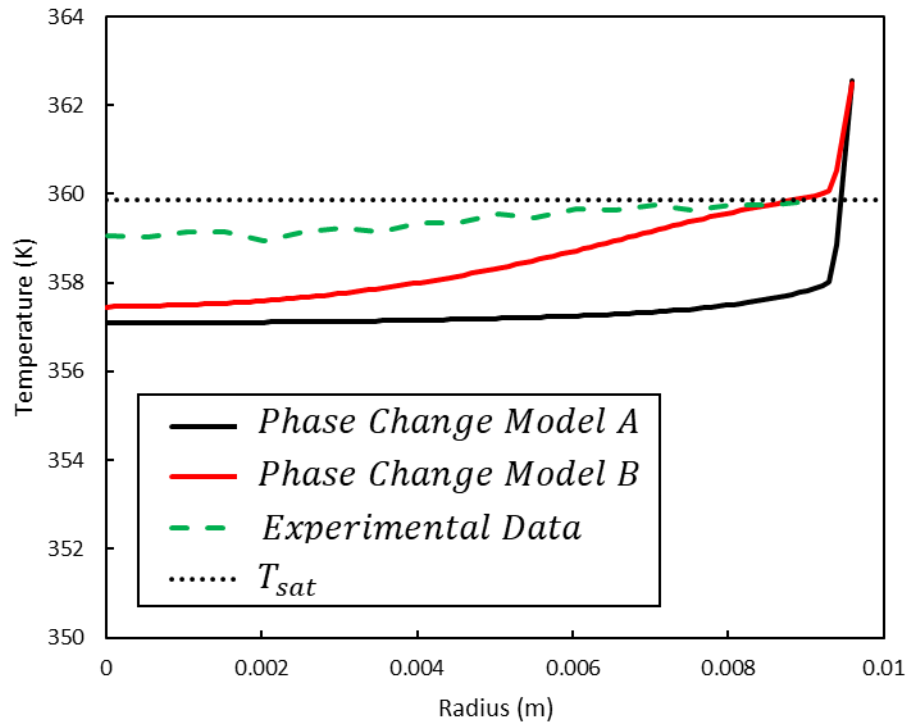


Figure 31 R12 temperature distribution for the different phase change models

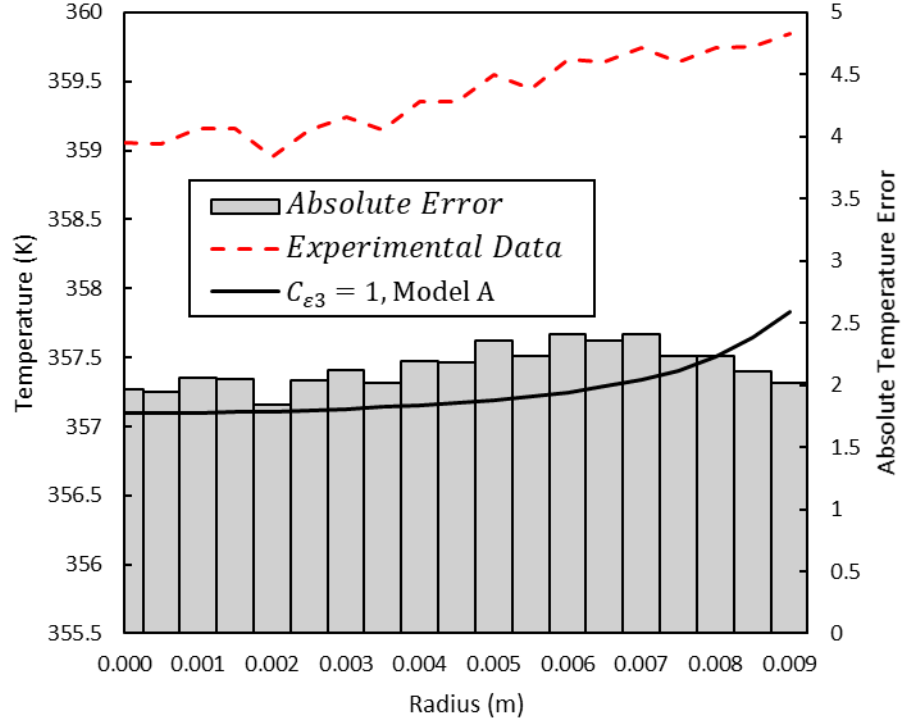


Figure 32 Comparison of numerical temperature results and experimental data

Figure 31 corresponds to the radial temperature distribution in the channel. The temperature output when using model B is more in line with the experimental data. Note that the inlet liquid temperature is not equal to the saturation temperature in the DEBORA 6 experiment (section 4.2.1). Hence, having a temperature lower than the saturation temperature is possible. Although not the best at predicting temperature, Model A yields a maximum of 2 Kelvin in absolute error when compared to the experiment (Figure 32). The overall better performance of Model A in the tested cases and its far superior prediction of radial gas void fraction distribution makes it the most favorable phase change model to use.

The analysis of the R12 case results confirmed the ability of the selected solver to simulate boiling flows. In addition, it helped us conclude the relationship between the turbulence quantities and the radial gas void fraction distribution.

5.2 CO₂ Results

In this section, CO₂ boiling flows in horizontal micro-channels are evaluated. For this case, the experimental data available is global. It is impossible, with the current technology, to get local experimental data in micro-scale channels. The main

parameter of interest is the pressure drop across a section of the horizontal channel. The initial tests are run on the 1 mm tube with a mass flux of $800 \text{ kg/m}^2\cdot\text{s}$ and a heat flux of 10 kW/m^2 (case 1 in Table 4). The experimental pressure drop is 0.03 bar for that case. The input mass flux is equal to $800 \text{ kg/m}^2\cdot\text{s}$ but at that section due to the experimental conditions the mass flux is shown to be slightly less.

5.2.1 Time and Mesh Sensitivity Analysis

Similarly to the R12 simulations, the time step is set as adaptive and is based on the maximum Courant Number as detailed in section 5.1.1

As the most important parameter in this case is the pressure drop, the mesh sensitivity analysis is conducted with respect to the pressure drop across a 200 mm section of the pipe corresponding to the experiment.

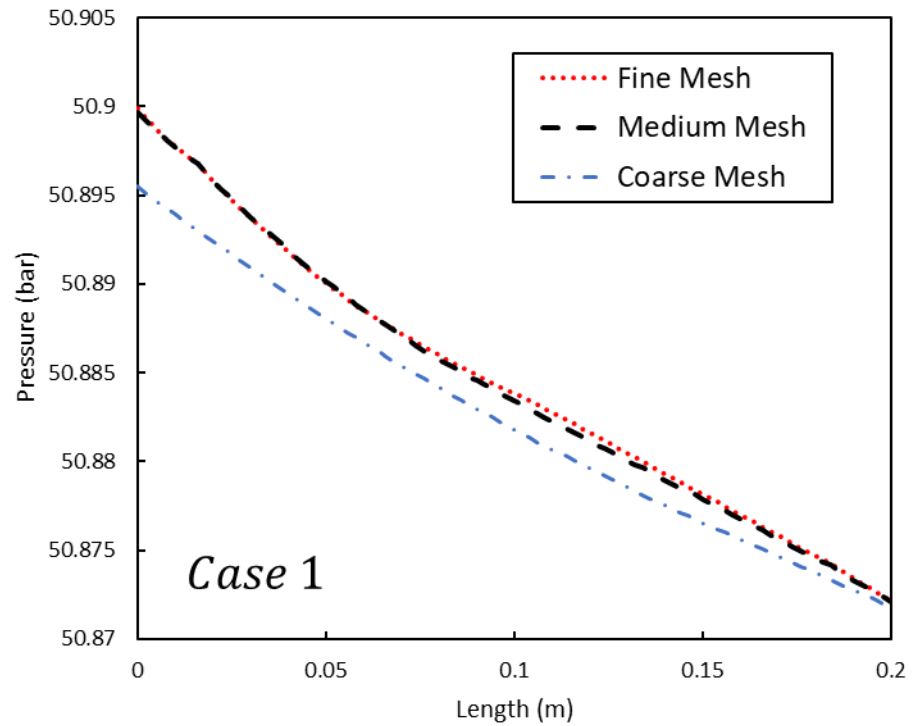


Figure 33 Pressure drop mesh sensitivity analysis for the CO₂ simulations

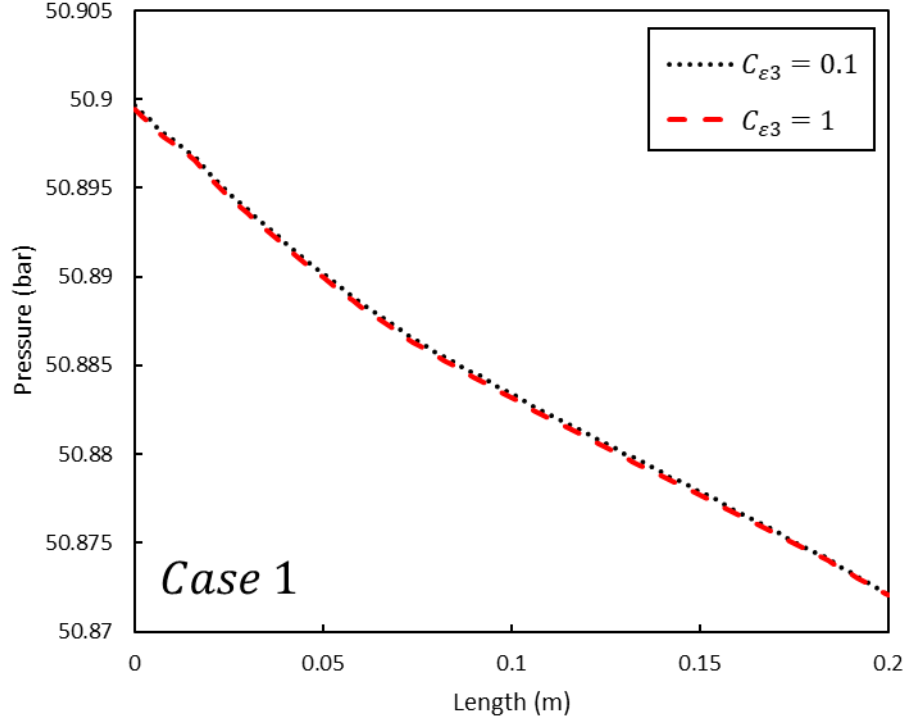


Figure 34 $C_{\epsilon 3}$ sensitivity analysis for the CO_2 microchannel simulations

Figure 33 shows the results of the mesh sensitivity analysis. The coarse mesh underestimates the pressure drop, while the medium mesh and fine mesh show pseudo-identical pressure fields and a maximum absolute error of 0.00437 bar. As a result, the medium mesh is the selected mesh. Another sensitivity analysis is conducted to check whether $C_{\epsilon 3}$ has any effect on the pressure drop. In micro-channels with low Reynolds number, as is our case, the turbulent viscosity is overshadowed by the molecular viscosity and surface tension forces. Figure 34 proves the aforementioned statement as the parameter $C_{\epsilon 3}$ does not have a major effect on the pressure drop. Taking into consideration that the first CFD simulation underestimated the pressure drop, $C_{\epsilon 3}$ equal 0.1 is chosen as the default value for the CO_2 simulations because it yields slightly higher pressure drop.

5.2.2 Pressure drop Results

To be able to assess the ability of the solver in predicting the pressure drop, six cases are simulated. These cases are shown in red in Figure 35, ID corresponds to the channel inner diameter and q to the heat flux. Only one case was simulated for a diameter of 2.15 mm as it considered a macro-scale channel.

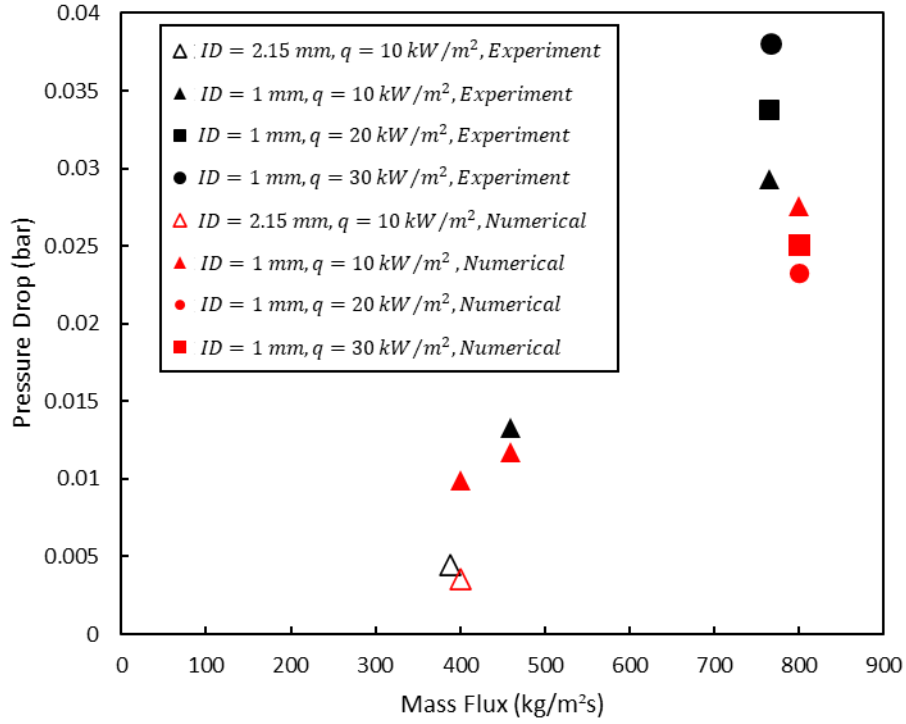


Figure 35 CO₂ pressure drop results for the 240 mm channel

Figure 35 shows the simulation results in terms of pressure drop. For the pressure drops of the cases where the heat flux is equal to 10 kW/m², the simulations yield a good agreement with the experimental data, with an accuracy near 93%. Those points are represented by the triangles. In micro-channels, as the heat flux increases, the pressure drop increases, for low vapour quality flows. The pressure drop increase is attributed to the increase in specific volume leading to higher flow velocities. However, as shown by the red square and red circle, the simulation is not following the expected trend.

When looking at the gas void fraction contours (Figure 36), the Leidenfrost effect seems to be preventing the mixing of the flow. This effect occurs when the temperature of the surface is hotter than the liquid's boiling point. A gas film is created separating the wall and the liquid. In that case, the fluid friction on the wall is mainly between the gas and the wall causing the underestimation of the pressure drop. This does not seem to happen in the case where the heat flux is 10 kW/m² providing a better prediction of the pressure drop. One way to solve this issue consists of adding a section after the heated section to the simulated channel so that the vapour quality of the flow is not compromised. By having a longer channel, the flow mixing is enhanced.

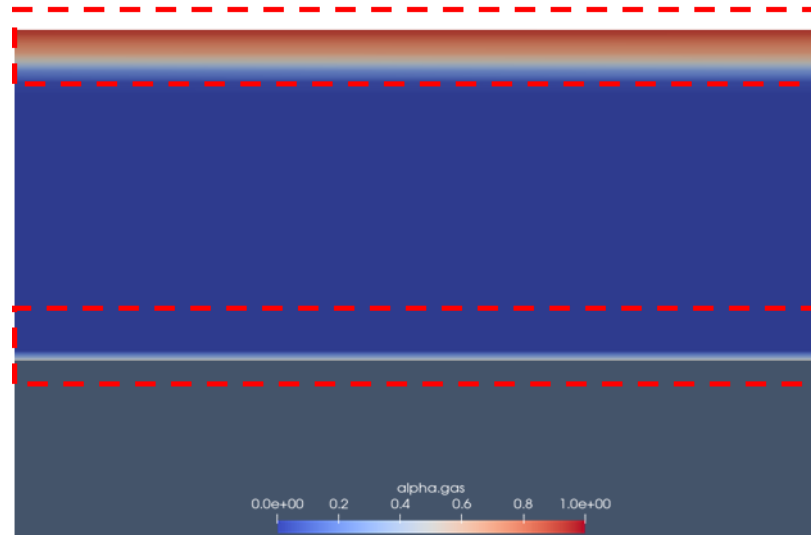


Figure 36 Visualization of Leidenfrost effect

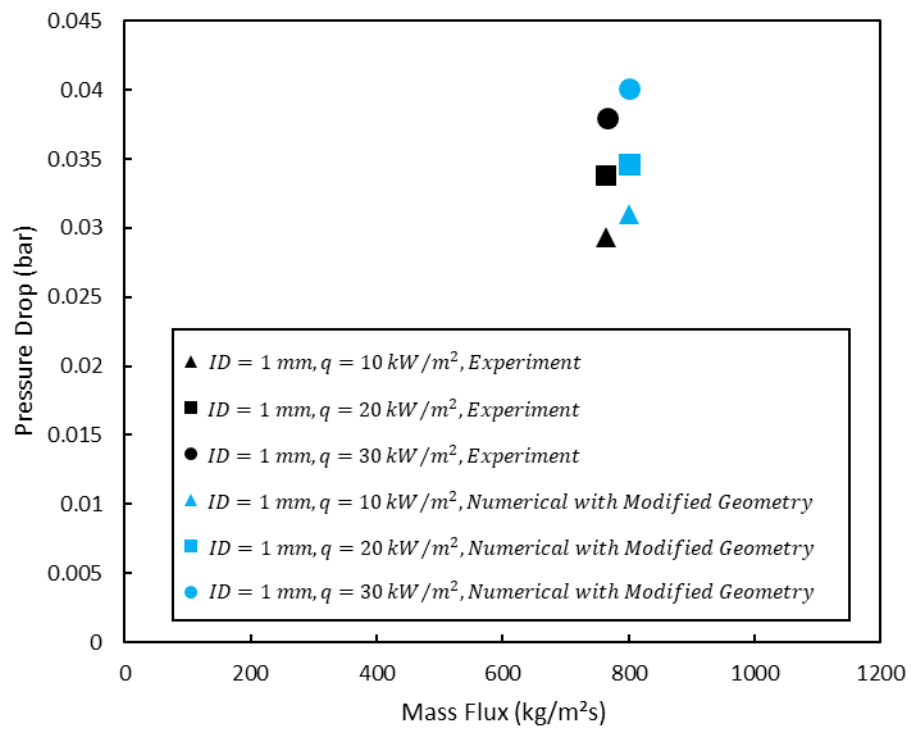


Figure 37 CO₂ pressure drop results for the 500 mm channel

Figure 37 shows the pressure drops in a 200 mm section upstream of the previous one to ensure better mixing. These simulations produce results that follow the experimental trend, and the results are within a 93% accuracy.

5.2.3 Evaluation of the CO₂ Flow at Different Sections

In order to understand this difference in behaviour in the upstream section (Figure 20), the void fraction compared to the gas velocity and the turbulence kinetic energy is evaluated.

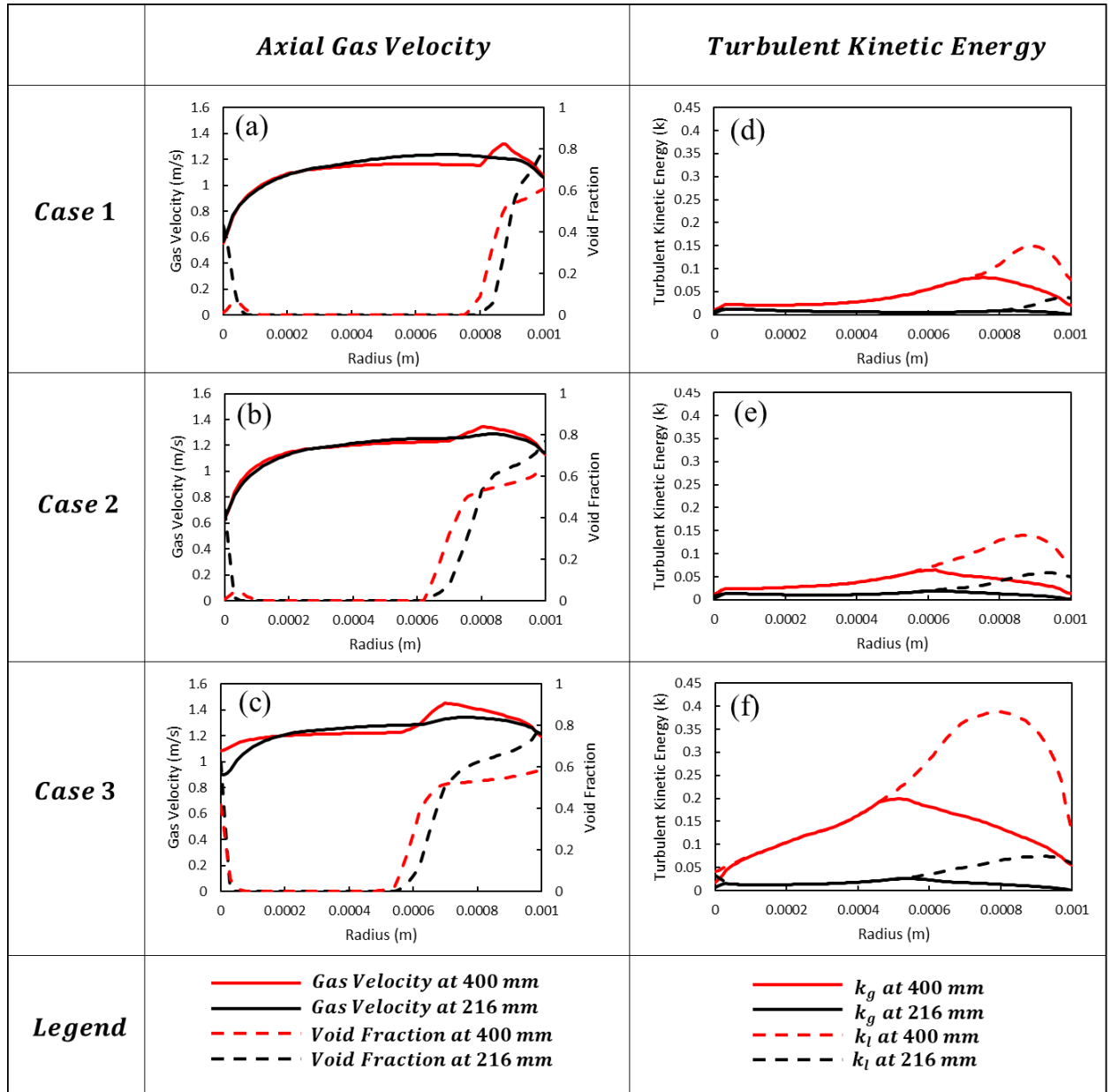


Figure 38 CO₂ void fraction and turbulent energy at different sections of the pipe

Figure 38 presents what is anticipated: the gas void fraction in the upstream section has a better distribution across the channel radius. Note that the gas film near the upper pipe wall is thicker due to buoyancy. The gas is created near the pipe wall then migrates to the upper part. This can also be noticed by the kink in the axial gas velocity near the

wall. This kink corresponds to an increase in momentum thus a decrease in the momentum thickness. This increase in momentum trails two phenomena. First, the increase in momentum flow rate increases the friction factor hence increasing the pressure drop. Secondly, this shift in momentum, leads to the production of more turbulent kinetic energy that has been proven in section 5.1.3 to play an important role in the migration of gas from the wall to the middle of the pipe; therefore, improving the mixing.

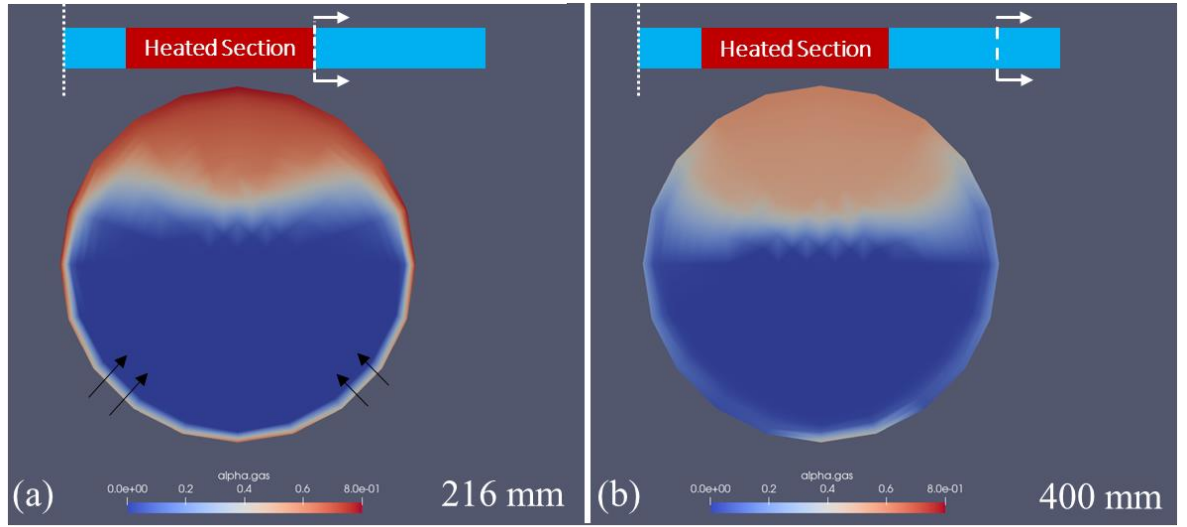


Figure 39 CO₂ void fraction visualization at different pipe sections

Figure 39 shows two slices of case 3. (a) is the section at 216 mm and (b) is the section at 400 mm. In (a), the flow is restricted to the wall with high gas void fractions across the pipe wall mimicking the Leidenfrost effect. In (b), a better flow mixture is displayed and the gas film around the channel walls is eliminated. As previously mentioned, the gas gathering in the top section of the tube is a result of the buoyancy forces.

To sum up, the R12 case was able to reveal a direct link between the turbulence quantities of the liquid and the formation and dissipation of gas. Additionally, it validated the use of reactingTwoPhaseEulerFoam for two-phase boiling flows. The CO₂ simulations proved the drawn relationship between the turbulence and the void fraction as well as showing the importance of having a more uniform mixture to better predict the pressure drops in two-phase boiling flows. The void fraction profiles across

the pipe radius displayed that buoyancy plays a major role in the distribution of gas in horizontal tubes.

Chapter 6

Conclusion

In conclusion, this thesis focuses on the simulation and understanding of the mechanics of boiling flows in macro and micro-scale channels. The turbulence quantities are evaluated, and the following conclusions are drawn:

In Macro-channels:

- Turbulence prediction in the liquid phase is critical to the mass transfer and not only the heat transfer:
 - The dissipation of turbulence in the liquid phase plays an important role in the phase change at the heated wall.
 - The production of turbulent kinetic energy in the liquid governs the transport of the gas in the radial direction.
- For low vapour quality flows, the turbulence quantities of the gas play a secondary role in mass and heat transfer.

In Micro-channels:

- For low Reynolds number two-phase flows, the turbulent stresses are overshadowed by the molecular stresses.
- Buoyancy is one of the main contributors in the migration of gas in the radial direction for horizontal pipes.
- The mixing between the two phases is crucial for the correct prediction of the flow characteristics.

Additionally, some CFD recommendations can be summarized as follows:

- It is crucial to use a two-equation turbulence model.
- Phase change is mainly driven by 3D effects.
- In the case of modelling boiling flows in micro-channels, the desired experimental data is, for example, the pressure drop distribution across the tube length, the temperature distribution across the pipe wall, the inlet turbulence level, the inlet vapour quality and some flow visualization.

References

- Antal, S. P., Lahey, R. T., & Flaherty, J. E. (1991). Analysis of phase distribution in fully developed laminar bubbly two-phase flow. *International Journal of Multiphase Flow*, 17(5), 635–652. [https://doi.org/10.1016/0301-9322\(91\)90029-3](https://doi.org/10.1016/0301-9322(91)90029-3)
- Bhanot, V., Petagna, P., Cioncolini, A., & Iacovides, H. (2020). Development and validation of a simulation tool for next generation detector cooling systems. *Nuclear Instruments and Methods in Physics Research, Section A: Accelerators, Spectrometers, Detectors and Associated Equipment*, 955(October 2019), 163264. <https://doi.org/10.1016/j.nima.2019.163264>
- Boussinesq, J. (1842-1929). A. du texte. (1897). *Théorie de l'écoulement tourbillonnant et tumultueux des liquides dans les lits rectilignes à grande section / par M. J. Boussinesq...* <https://gallica.bnf.fr/ark:/12148/bpt6k9738517t>
- Burns, A. D., Frank, T., Hamill, I., & Shi, J. M. (2004). The Favre averaged drag model for turbulent dispersion in Eulerian multi-phase flows. *5th International Conference on Multiphase Flow*, 392, 1–17. http://www.drthfrank.de/publications/2004/Burns_Frank_ICMF_2004_final.pdf
- Cappelli. (2018). CFD with OpenSource software A detailed description of reactingTwoPhaseEulerFoam focussing on the links between mass and heat transfer at the interface Learning outcomes. *CFD with OpenSource Software A*, 1–34.
- Collier, J. G., & Thome, J. R. (1994). Convective Boiling and Condensation. In *Journal of Fluid Mechanics* (Third Edit). Oxford University Press. <https://doi.org/10.1017/S0022112095233160>
- Drew, D. A., & Lahey, R. T. (1987). The virtual mass and lift force on a sphere in rotating and straining inviscid flow. *International Journal of Multiphase Flow*, 13(1), 113–121. [https://doi.org/10.1016/0301-9322\(87\)90011-5](https://doi.org/10.1016/0301-9322(87)90011-5)
- Ganapathy, H., Shooshtari, A., Choo, K., Dessiatoun, S., Alshehhi, M., & Ohadi, M. (2013). Volume of fluid-based numerical modeling of condensation heat transfer and fluid flow characteristics in microchannels. *International Journal of Heat and Mass Transfer*, 65, 62–72. <https://doi.org/10.1016/j.ijheatmasstransfer.2013.05.044>
- Garnier, J., Manon, E., & Cubizolles, G. (2001). Local measurements on flow boiling of refrigerant 12 in a vertical tube. *Multiphase Science and Technology*, 13(1–2), 1–111. <https://doi.org/10.1615/multscientechn.v13.i1-2.10>
- Hellenschmidt, D., & Petagna, P. (2020). Effects of saturation temperature on the boiling properties of carbon dioxide in small diameter pipes at low vapour quality: Pressure drop. *International Journal of Heat and Mass Transfer*, 163. <https://doi.org/10.1016/j.ijheatmasstransfer.2020.120209>
- Kadhum, M. H. (2016). *Exhaust Heat Recovery Techniques of Internal Combustion Engines by Organic Rankine Cycle*. November.

- Karayiannis, T. G., & Mahmoud, M. M. (2017). Flow boiling in microchannels: Fundamentals and applications. *Applied Thermal Engineering*, 115, 1372–1397. <https://doi.org/10.1016/j.applthermaleng.2016.08.063>
- Krepper, E., & Rzehak, R. (2011). CFD for subcooled flow boiling: Simulation of DEBORA experiments. *Nuclear Engineering and Design*, 241(9), 3851–3866. <https://doi.org/10.1016/j.nucengdes.2011.07.003>
- Kurul, N., & Podowzki, M. Z. (1991). On the Modeling of Multidimensional Effects in Boiling Channels. *Proceedings of the 27th National Heat Transfer Conference*.
- Lahey, R. T. (2005). The simulation of multidimensional multiphase flows. *Nuclear Engineering and Design*, 235(10–12), 1043–1060. <https://doi.org/10.1016/j.nucengdes.2005.02.020>
- Magnini, M., Pulvirenti, B., & Thome, J. R. (2013). Numerical investigation of hydrodynamics and heat transfer of elongated bubbles during flow boiling in a microchannel. *International Journal of Heat and Mass Transfer*, 59(1), 451–471. <https://doi.org/10.1016/j.ijheatmasstransfer.2012.12.010>
- Magnini, M., & Thome, J. R. (2016). A CFD study of the parameters influencing heat transfer in microchannel slug flow boiling. *International Journal of Thermal Sciences*, 110, 119–136. <https://doi.org/10.1016/j.ijthermalsci.2016.06.032>
- Mastrullo, R., Mauro, A. W., Rosato, A., & Vanoli, G. P. (2010). Carbon dioxide heat transfer coefficients and pressure drops during flow boiling: Assessment of predictive methods. *International Journal of Refrigeration*, 33(6), 1068–1085. <https://doi.org/10.1016/j.ijrefrig.2010.04.005>
- Morel, C. (2015). *Mathematical Modeling of Disperse Two-Phase Flows* (Vol. 114). <http://link.springer.com/10.1007/978-3-319-20104-7>
- Schiller, L., & Naumann, A. (1935). *A drag coefficient correlation*. 77, 318–320.
- Tomiyama, A., Tamai, H., Zun, I., & Hosokawa, S. (2002). Transverse migration of single bubbles in simple shear flows. *Chemical Engineering Science*, 57(11), 1849–1858. [https://doi.org/10.1016/S0009-2509\(02\)00085-4](https://doi.org/10.1016/S0009-2509(02)00085-4)
- Yao, W., & Morel, C. (2002). Prediction of parameters distribution of upward boiling two-phase flow with two-fluid models. *International Conference on Nuclear Engineering, Proceedings, ICONE*, 3(June), 801–808. <https://doi.org/10.1115/ICONE10-22463>
- Zaepffel, D. (2012). *Modélisation des écoulements bouillants à bulles polydispersées*
To cite this version : HAL Id : tel-00682899.
- Zhou, S., Xu, X., & Sammakia, B. G. (2013). Modeling of boiling flow in microchannels for nucleation characteristics and performance optimization. *International Journal of Heat and Mass Transfer*, 64, 706–718. <https://doi.org/10.1016/j.ijheatmasstransfer.2013.05.031>
- Zhuan, R., & Wang, W. (2012). Flow pattern of boiling in micro-channel by numerical simulation. *International Journal of Heat and Mass Transfer*, 55(5–6), 1741–1753. <https://doi.org/10.1016/j.ijheatmasstransfer.2011.11.029>

Appendix A

Experimental Data from DEBORA 6

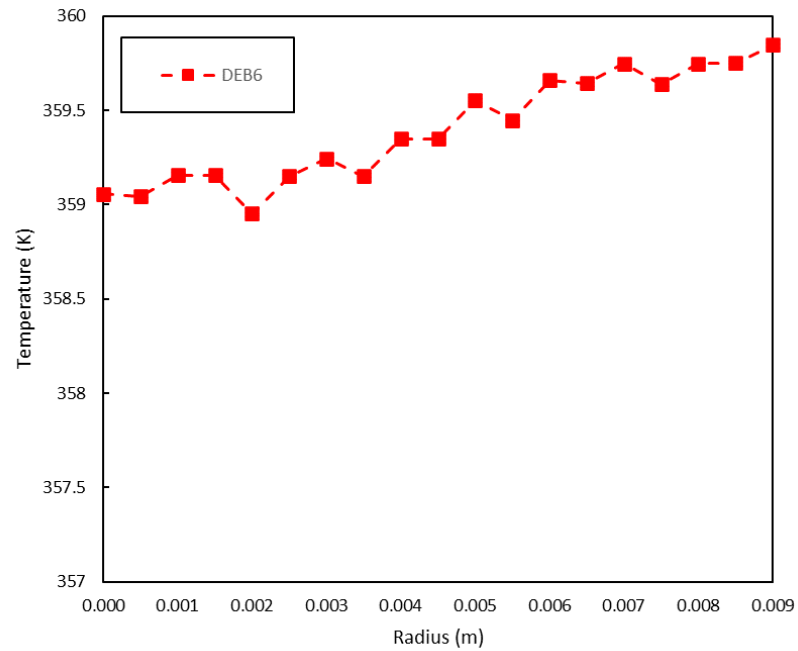


Figure 40 DEBORA 6 radial temperature distribution

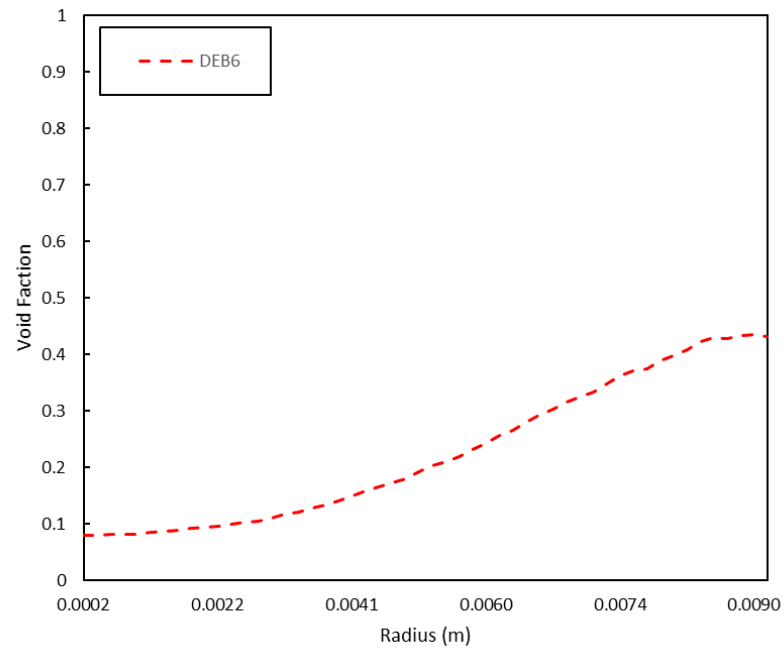


Figure 41 DEBORA 6 radial gas void fraction distribution

Appendix B

Experimental Data from CERN

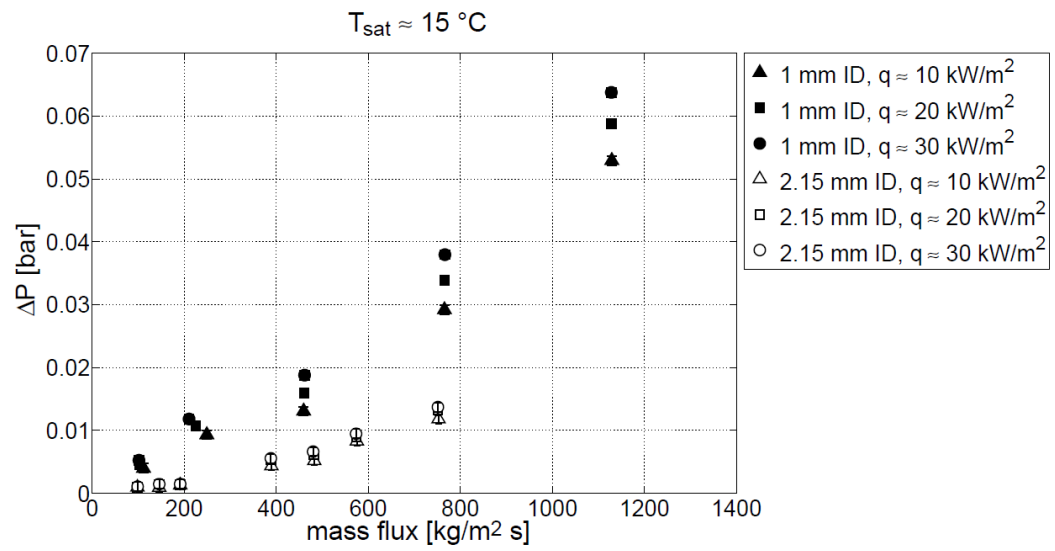


Figure 42 CO₂ pressure drop experimental data

Appendix C

Error Equations

Absolute Error (AE)

$$AE = | \textit{Experimental Data} - \textit{Numerical Data} | \quad (33)$$

The experimental and numerical data points need to be assessed at the same position. In the case of this thesis, the two data points are at the same radial position.

Root Relative Squared Error (RRSE)

$$RRSE = \sqrt{\frac{\sum_{i=1}^n (x_i - r_i)^2}{\sum_{i=1}^n r_i^2}} \quad (34)$$

Where i , n , x_i and r_i are the position of a data point in the radial direction, the total number of evaluated data points, the numerical results at position i and the experimental data at position i , respectively.